

ON THE ORIGIN OF THE MULTI-GEV PHOTONS FROM THE CLOSEST BURST
WITH INTERMEDIATE LUMINOSITY: GRB 190829AN. FRAIJA^{1†}, P. VERES², P. BENIAMINI³, A. GALVAN-GAMEZ¹, B. D. METZGER^{4,5}, R. BARNIOL DURAN⁶ AND R. L. BECERRA¹¹Instituto de Astronomía, Universidad Nacional Autónoma de México, Apdo. Postal 70-264, Cd. Universitaria, Ciudad de México 04510²Center for Space Plasma and Aeronomic Research (CSPAR), University of Alabama in Huntsville, Huntsville, AL 35899, USA³TAPIR, Mailcode 350-17, California Institute of Technology, Pasadena, CA 91125, USA⁴Columbia Astrophysics Laboratory, Columbia University, New York, NY 10027, USA⁵Center for Computational Astrophysics, Flatiron Institute, New York, NY 10010, USA and⁶Department of Physics and Astronomy, California State University, Sacramento, 6000 J Street, Sacramento, CA 95819-6041, USA*Draft version January 22, 2022*

ABSTRACT

Very-high-energy (VHE) emission is usually interpreted in the synchrotron-self Compton (SSC) scenario, and expected from the low-redshift and high-luminosity gamma-ray bursts (GRBs), as GRB 180720B and GRB 190114C. Recently, VHE emission was detected by the H.E.S.S. telescopes from one of the closest burst GRB 190829A which was associated with the supernova (SN) 2019oyw. In this paper, we present a temporal and spectral analysis from optical bands to Fermi LAT energy range over multiple observational periods beginning just after the BAT trigger time and extending for almost three months. We show that the X-ray and optical observations are consistent with synchrotron forward-shock emission evolving between the characteristic and cooling spectral breaks during the early and late afterglow in a uniform-density medium. Modelling the light curves together with its spectral energy distribution, it is shown that the outflow expands with an initial bulk Lorentz factor of $\Gamma \sim 30$, which is high for a low-luminosity GRBs and low for a high-luminosity GRBs. The values of the initial bulk Lorentz factor and the isotropic equivalent energy suggest that GRB 190829A is classified as an intermediate-luminosity burst and consequently, it becomes the first burst of this class in being detected in the VHE gamma-ray band by an imaging atmospheric Cherenkov telescope, and, in turn, the first event without being simultaneously observed by the Fermi LAT instrument. Analyzing the intermediate-luminosity bursts with $z \lesssim 0.2$ such as GRB 130702A, we show that bursts with intermediate luminosity are potential candidates to be detected in very-high energies.

Subject headings: Gamma-rays bursts: individual (GRB 190829A) — Physical data and processes: acceleration of particles — Physical data and processes: radiation mechanism: nonthermal — ISM: general - magnetic fields

1. INTRODUCTION

Observational evidence has firmly established that gamma-ray bursts (GRBs) lasting longer than few seconds are associated to the core collapse (CC) of massive stars (Woosley 1993) leading to supernovae (SNe; Galama et al. 1998; Bloom et al. 1999; Woosley and Bloom 2006). Based on the isotropic equivalent luminosity in the gamma-ray band and the opening angle, some authors have classified CC-SNe as low-luminosity (ll)GRBs with $L_{\text{iso}} \lesssim 10^{48.5} \text{ erg s}^{-1}$, intermediate-luminosity (il)GRBs with $10^{48.5} \lesssim L_{\text{iso}} \lesssim 10^{49.5} \text{ erg s}^{-1}$ and high-luminosity (hl)GRBs with $L_{\text{iso}} \gtrsim 10^{49.5} \text{ erg s}^{-1}$ (Bromberg et al. 2011; Hjorth 2013; Cano et al. 2017). Whereas llGRBs are associated with the shock breakout¹ and characterized by having opening angles $\gtrsim 30^\circ$, and hlGRBs with an emerging collimated jet (Bromberg et al. 2011), there is no clear association for ilGRBs (Schulze et al. 2014). To date, there are eight confirmed GRB-SNe detected within $z \lesssim 0.2$: GRB 980425/ SN 1998bw (Galama et al. 1998), GRB 060218/ SN 2006aj (Campana and et al. 2006), GRB 100316D/ SN 2010bh (Cano et al. 2011) and GRB 171205A/ SN 2017iuk (Izzo et al. 2019) classified as llGRBs, GRB 130702A/ SN 2013dx (D’Elia et al. 2015) as ilGRB and

GRB 030329/SN 2003dh (Hjorth et al. 2003) as hlGRB.²

Very-high-energy (VHE $\geq 10 \text{ GeV}$) photons are expected from low-redshift and high-luminosity bursts (Wang et al. 2019; Fraija et al. 2019a). During the afterglow phase electrons are shock-accelerated and cooled down by synchrotron process that radiates photons from radio to gamma-rays. The maximum photon energy radiated by the synchrotron process during the deceleration phase becomes $\sim 5 - 10 \text{ GeV} \left(\frac{\Gamma(t)}{100} \right) (1+z)^{-1}$, where $\Gamma(t)$ is the bulk Lorentz factor (decaying with time) and z is the redshift (Piran and Nakar 2010; Abdo et al. 2009; Barniol Duran and Kumar 2011). Another cooling process is the synchrotron self-Compton (SSC) emission, synchrotron photons are scattered above tens of GeVs by the same electron population (Zhang and Mészáros 2001; Fraija et al. 2019a; Fraija 2015; Fraija et al. 2017a). This is the case of GRB 180720B and GRB 190114C which showed similarities to other hlGRBs detected by Fermi LAT (Ajello et al. 2019). These bursts were detected by the Major Atmospheric Gamma Imaging Cherenkov (MAGIC; Acciari et al. 2019) and the High Energy Stereoscopic System (H.E.S.S.; Abdalla et al. 2019) telescopes at energies above 100 GeV, respectively. The high-energy photons detected by Fermi LAT beyond the synchrotron limit

[†] nifraija@astro.unam.mx¹ If llGRBs are shock breakouts, then one should distinguish between the injected luminosity and the observed one, since they will be very different.² Due to the luminosity and opening angle, GRB 161219B/SN 2016jca cannot be classified as low- or intermediate-lGRB (Cano et al. 2017; Ashall et al. 2019).

together with the VHE photons reported by H.E.S.S. and MAGIC telescopes were interpreted in the SSC scenario during the afterglow phase (Fraija et al. 2019b,a; Zhang 2019). On the other hand, in the case of IIGRBs which are characterized by being less energetic (Bromberg et al. 2011), high-energy photons in the energy range of the Fermi LAT are hardly expected. An interesting case study in this aspect is il-GRBs which have luminosities between low- and high-IIGRBs (D’Elia et al. 2015; Cano et al. 2017).

The Burst Area Telescope (BAT) instrument on-board the Swift satellite triggered on GRB 190829A at 2019 August 29 19:56:44.60 UT (Dichiara et al. 2019). The H.E.S.S. telescopes followed-up the afterglow of GRB 190829A. A preliminary onsite analysis of these observations showed a $> 5\sigma$ gamma-ray excess in coincidence with the direction of GRB 190829A (de Naurois and H. E. S. S. Collaboration 2019). This burst associated with a SN type Ic-BL (de Ugarte Postigo et al. 2019) was followed up by a large-scale campaign with several instruments onboard satellites and ground telescopes that covered most of the electromagnetic spectrum. Recently, Chand et al. (2020) discussed the VHE emission detected from GRB 190829A in terms of the low-luminosity bursts and shock breakout scenario.

GRB 130702A classified as an intermediate-luminosity burst and associated to a broad-line, type Ic supernovae SN2013dx (D’Elia et al. 2015), was detected at different wavelengths ranging from radio to high-energy gamma-rays. The Gamma-ray Burst Monitor (GBM) instrument on-board the Fermi satellite triggered on GRB 130702A at 2013 July 02 00:05:23.079 UTC. The Fermi LAT instrument detected photons from this burst above >100 MeV within 2200 s. Details of the data analysis and the afterglow observations are reported in D’Elia et al. (2015) and Toy et al. (2016).

In this paper, we present a detailed data analysis of the multi-wavelength observations of GRB 190829A. Using the best-fit parameters found after modelling the X-ray and optical light curves of this burst, we analyze the VHE emission reported by the H.E.S.S. experiment. Our model is generalized to study the mechanism involved to interpret the high-energy photons around other ilGRB (e.g. GRB 130207A). The paper is arranged as follows. In Section 2 we present multi-wavelength observations and data reduction. In Section 3 we model and interpret the multi-wavelength observations. In Section 4 we discuss our results around GRB 190829A. In Section 5 we present the analysis and discussion of the multi-GeV photons reported in GRB 190829A and GRB 130702A and finally, in Section 5 we give a brief summary. The convention $Q_x = Q/10^x$ in cgs units will be adopted through this paper.

2. GRB 190829A

2.1. Observations and data reduction

2.1.1. Fermi: GBM observations

The Fermi GBM instrument triggered and localized GRB 190829A at 2019 August 29 19:55:53.13 UT. GBM data is analyzed using the public database at the Fermi website.³ Flux values are derived using the spectral analysis package Rmfit version 432.⁴ The time tagged event (TTE) files of the NaI detectors (5, 6, 7 and 9) and the BGO detector B1 are used to analyze the GBM data. Table 1 corresponds to the values of the spectral analysis of GRB 190829A using

GBM data during the time interval $[-2.0; 68.0]$ s. During this interval, an initial pulse followed by a brighter peak are observed: the initial pulse between $[-2.0; 12.0]$ s and the brighter peak between $[46.0; 68.0]$ s which correspond to total isotropic energies of $E_{\gamma, \text{iso}} = (9.151 \pm 0.504) \times 10^{49}$ erg and $(2.967 \pm 0.032) \times 10^{50}$ erg, respectively, and peak energies of (67.88 ± 23.3) keV and (11.47 ± 0.360) keV, respectively. These are calculated considering the energy range of 1 keV - 10 MeV. This table shows the time interval (column one), low-energy (column 2) and high-energy (column three) spectral indexes of the Band function, the peak energy (column four), the isotropic-equivalent energy (fifth column) and the observed flux (last column). Although the power law with exponential cutoff (CPL), the blackbody (BB, Planck function) and the Band function (Band et al. 1993) are considered, the time-resolved spectra best fit to the Band function. This model is preferred over both the CPL and the BB models. To assess the quality of a spectral fit, the traditional χ^2 statistics is used. We want to emphasize that a thermal photospheric emission in the GBM data is not observed.

2.1.2. Fermi: LAT observations

The Fermi LAT instrument performed a search for high-energy emission on different time windows around the position of this burst and upper limits with a 95% confidence level in the 0.1 - 1 GeV energy range were derived (Piron et al. 2019). Considering a PL function $\propto \epsilon_{\gamma}^{-\Gamma_{\text{LAT}}}$ with a photon index of $\Gamma_{\text{LAT}} = \beta_{\text{LAT}} + 1 = 2.0$, the derived LAT upper limits were 5.3×10^{-10} , 3.2×10^{-10} , 1.4×10^{-10} and 1.8×10^{-10} erg cm $^{-2}$ s $^{-1}$ for time windows of 0 - 1.1, 0 - 10, 10 - 30 and 15 - 30 ks, respectively.

2.1.3. Swift: UVOT observations

The Swift UVOT started settled observations of the field of view of this burst 106 s after the BAT trigger time (Oates et al. 2019). This instrument detected an emission consistent with the afterglow in the V, B, White and U bands. Analyzing the afterglow spectrum, Valeev et al. (2019) found absorption lines of Ca, H and K doublet, identifying this burst with DSS galaxy J025810.28-085719.2 at a redshift of $z = 0.0785 \pm 0.005$. The UVOT data is obtained using the public available database at the official Swift website.⁵ The observed fluxes and their corresponding uncertainties used in this work are calculated using the standard conversion for AB magnitudes shown in Fukugita et al. (1996). The optical data is corrected by the galactic extinction using the relation derived in Becerra et al. (2019). The values of $\beta_{\text{O}} = 0.48$ for optical filters and a reddening of $E_{B-V} = 0.05$ (Dichiara et al. 2019) are used.

2.1.4. Swift: BAT and XRT observations

The Swift BAT instrument triggered on GRB 190829A at 2019 August 29 19:56:44.60 UT (Dichiara et al. 2019). The instrument located this burst with coordinates RA(J2000)=02h 58m 10s and Dec=-08d 58' 03" with

³ <http://fermi.gsfc.nasa.gov/ssc/data>

⁴ <https://fermi.gsfc.nasa.gov/ssc/data/analysis/rmfit/>

⁵ <https://www.swift.ac.uk/archive/obs.php>

an uncertainty of 3 arcmin. The Swift XRT instrument started detecting GRB 190829A at 19:58:21.9 UT, 97.3 s after the BAT trigger. This instrument monitored GRB 190829A in the Windowed Timing (WT) mode with a spectrum exposure of 128 s and the Photon Counting (PC) mode with a spectrum exposure of 10.8 ks. Swift data is obtained using the publicly available database at the official Swift website.⁶ The flux density at 10 keV is transformed to 1 keV using the conversion factor derived in [Evans et al. \(2010\)](#).

2.1.5. H.E.S.S.: VHE gamma-ray observations

H.E.S.S. telescopes reported the detection of VHE gamma-ray emission compatible with the direction of GRB 190829A ([de Naurois and H. E. S. S. Collaboration 2019](#)). This emission lasting 3.9 hours was detected with a significance 5σ at 4.3 hours after the BAT trigger time.

2.1.6. GRB / SN observations

GROND, mounted at the 2.2m MPG telescope at ESO La Silla Observatory, found a relatively sharp growth in all bands between 4.5 and 5.5 days after the trigger time ([Bolmer et al. 2019](#)). [Terreran et al. \(2019\)](#) studied the spectrum of the optical afterglow with the Low Resolution Imaging Spectrometer (LRIS). Authors found identical features consistent with a broad-line SN and with the X-ray analysis reported by [Osborne et al. \(2019\)](#). In addition, [de Ugarte Postigo et al. \(2019\)](#) found evidence of broad absorption lines with expansion velocities similar to SN 1998bw. It confirmed the association of the SN 2019oyw classified as Type Ic-BL⁷ with GRB 190829A.

2.2. Analysis of the multi-wavelength observations

2.2.1. GBM data analysis

The upper left-hand panel in Figure 1 shows the gamma-ray light curve and the evolution of the peak energy (E_{peak}), the low-energy (α_{Band}) and high-energy (β_{Band}) spectral indexes of GRB 190829A. The initial gamma-ray pulse is shown in open circles and the brighter peak in filled circles. These sub-panels are ordered from top to bottom: the low-energy spectral index, the high-energy spectral index, the energy peak and the gamma-ray light curve obtained in the 10 - 1000 keV energy range. In order to fit the entire gamma-ray light curve, we use the functions given by $F_{\nu}(t) \propto e^{-\frac{t-t_0}{\tau_1}} F_k$ with $F_k = e^{-\frac{t-t_0}{\tau_2}}$ ([Norris et al. 2005](#)) for the initial pulse and $F_k = (\frac{t-t_0}{t_0})^{-\alpha_{\gamma}}$ ([Vestrand et al. 2006](#)) for the brighter peak. The terms t_0 is the starting time, $\tau_{1(2)}$ is the timescale of the flux rise (decay) and α_{γ} the power index of fast decay. To fit the evolution of the parameters (E_{peak} , α_{Band} and β_{Band}), we use PL functions $\propto t^{-\delta}$ with δ the power index. The Chi-square (χ^2) minimization method, developed in the ROOT software package ([Brun and Rademakers 1997](#)) is used to find the best-fit values which are reported in Table 2. In order to find the minimum variability timescale for this burst, the method utilized by [Bhat et al. \(2012\)](#) is used. This variability timescale corresponds to (214.7 ± 6.9) ms.

2.2.1.1. Evolution of the spectral parameters — During the first pulse, we found that the lower-energy photon index is around $\alpha_{\text{Band}} \approx -0.1$ which is much harder than the typical value ($\alpha_{\text{Band}} \approx -1$) and also beyond the so-called “synchrotron line of death” ($-\frac{2}{3}$; [Preece et al. 1998](#)). While the spectrum parameters might indicate a contribution of thermal emission ([Zhang et al. 2018](#); [Ryde et al. 2010](#); [Mészáros and Rees 2000](#)), magnetic dissipation ([Beniamini and Piran 2014](#); [Beniamini et al. 2017, 2018](#)) or “jitter” (a variant of the synchrotron) radiation mechanism ([Medvedev 2000](#)), the lower-energy photon index here is not well constrained, because the peak energy is very low, and the photons that were supposed to constrain α_{Band} fall out of the GBM range. The scenarios of the jitter radiation and thermal emission are disfavored. The jitter due to the assumed small coherence scale (λ_B) is not revealed from particle-in-cell (PIC) numerical simulations of relativistic shocks ([Spitkovsky 2008a,b](#)) and the thermal emission due to the rapid variation of the energy peak ([Ryde and Pe’er 2009](#)).⁸

During the brighter gamma-ray peak the Band-function parameters are typical and similar to most bursts ($\alpha_{\text{Band}} \approx -1.1$ and $\beta_{\text{Band}} \approx -2.5$). The value of low-energy spectral index of ~ -1 can be interpreted as synchrotron emission in a decay magnetic field ([Uhm and Zhang 2014](#)), magnetic reconnections/dissipations ([Beniamini and Piran 2014](#); [Beniamini et al. 2017, 2018](#); [Lazarian et al. 2019](#)) and dissipative photosphere models ([Pe’er et al. 2006](#); [Lazzati and Begelman 2010](#); [Vurm and Beloborodov 2016](#); [Ahlgren et al. 2015](#)). It is also possible to have a combination of synchrotron and photospheric components that evolve differently with time (e.g. [Beniamini and Giannios 2017](#)).

2.2.2. Fermi data Analysis

The upper right-hand panel in Figure 1 shows the upper limits and the VHE emission in the range reported by H.E.S.S. In order to obtain high-energy photons with energies above ≥ 100 MeV, we analyze the data files of GRB 190829A which are given at the data website.⁹ Details of the Fermi tools and the procedure performed to analyze the Fermi LAT data are presented in [Fraija et al. \(2019b\)](#). Our analysis indicates that there are no photons associated to GRB 190829A with a probability larger than 95%.

2.2.3. UVOT data analysis

The lower left-hand panel in Figure 1 shows the UV/optical light curves of GRB 190829A with the best-fit curves using broken power-law (BPL) functions. The light curves of the Swift UVOT obtained in the V, B, White and U bands display that before ≈ 700 s all color filters remain constant, after they increase as $F_{\nu} \propto t^{-\alpha_0}$ with $\alpha_0 \approx -3$, reaching the maximum values at $\approx 1.4 \times 10^3$ s, and finally these begin to decrease with slopes of $\alpha_0 \approx 1$ up to $\sim 3 \times 10^4$ s. After all this time, the flux densities in all color filters become constant, dominated by the host galaxy. The corresponding best-fit values of each color filter as well as the timescales of $\Delta t/t$ ([Chincarini et al. 2007](#)) are reported in Table 3. The timescales of $\Delta t/t$ are calculated using Δt the full width at

⁶ https://www.swift.ac.uk/burst_analyser/00922968/

⁷ <http://www.rochesterastromy.org/snimages/>

⁸ Authors studied the evolution of the temperature in 49 individual time-resolved pulses. They reported that during the first seconds the temperature is almost constant and after decay as a PL with a sample-averaged temporal index of 0.68.

⁹ <https://fermi.gsfc.nasa.gov/cgi-bin/ssc/LAT/LATDataQuery.cgi>

half-maximum (FWHM; Chincarini et al. 2007) adopting a Gaussian width and t obtained at the maximum value of the flux.

2.2.4. BAT and XRT data analysis

The lower right-hand panel in Figure 1 shows the X-ray light curves (top), the spectral evolution of the photon index (medium) and hardness ratio (bottom). The X-ray light curve in the main panel is shown at 1 keV. Five epochs, labeled as “0”, “I”, “II”, “III” and “IV” corresponding to the time intervals [52; 62] s, [132; 267] s, [267; 752] s, [752; 1.4×10^5] s and $> 1.4 \times 10^5$, respectively, are identified.¹⁰ A precursor can be identified in this panel ~ 3 s after the GBM trigger time. The dashed lines in gray color represent the best-fit curves reported by Swift team.¹¹ All the epochs are fitted with PL functions $\propto t^{-\alpha}$. The epoch “0” corresponds to the prompt emission fitted with a temporal index of $\alpha_{X,I} = 2.73 \pm 0.28$. The steep decay in epoch “I” is fitted with a temporal index of $\alpha_{X,I} = 3.53 \pm 0.70$ and the subsequent very shallow decay identified in epoch “II” is described with the temporal index of $\alpha_{X,II} = 0.06 \pm 0.05$. In epoch “III” the X-ray flare is modelled with a rising slope of $\alpha_{X,III,rise} = -(3.12 \pm 0.94)$, corresponding to a timescale of $\Delta t/t = 0.75 \pm 0.24$. Finally, the canonical normal decay in epoch “IV” is described using the values reported by the Swift analysis; a temporal index of $\alpha_{X,IV} = 1.23 \pm 0.04$ after the break time of $t_{br} = 1.4^{+0.17}_{-0.15} \times 10^5$ s. The best-fit values of the X-ray data are reported in Table 4.

During the epoch “I” and “II” (see the small box), the X-ray light curve at 10 keV displays several peaks labelled as “a”, “b”, “c”, “d”, “e”, “f”, “g”, “h” and “i”. The best-fit values of the rising and falling slopes with their corresponding timescales are reported in Table 5.

Figure 2 shows the spectral energy distribution (SED) of GRB 190829A built with the optical and X-ray data at two different times (epoch “III”); 6.0×10^3 s (left) and 1.8×10^4 s (right). These SEDs are modelled with SPLs with spectral indexes of $\beta_X = 0.48 \pm 0.05$ and $\beta_X = 0.47 \pm 0.05$, respectively. The gray dashed lines correspond to the best-fit curves obtained from XSPEC for a column density of $(7.9 \pm 0.6) \times 10^{21} \text{ cm}^{-2}$. On the other hand, we analyze XRT data in the PC and WT mode with a PL and a BB model incorporated in XSPEC v.12.10.1 (Arnaud 1996) in 13 time windows between 100 s and 1700 s, as shown in Table 6. This table shows the best-fit values using the PL and the PL plus BB model. It can be seen that although in some time windows the traditional χ^2 statistics is slightly better when a BB model is introduced, there is no clear evidence of the existence of a thermal component.

2.2.4.1. The photon index and hardness ratio light curves— The lower right-hand panel in Figure 1 shows the spectral index (Γ_{ph} ; medium) and hardness ratio (H_R ; bottom) light curves. The hardness ratio for the BAT data is defined by the photon flux in the ranges (25 - 50 keV)/(15 - 25 keV) and for XRT data in the ranges (1.5 - 10 keV)/(0.3 - 1.5 keV) (Evans et al. 2010). We analyze the evolution of the photon index and hardness ratio in each epoch.

Epoch “0”. During the prompt emission it can be noted that the photon index and the hardness ratio exhibit a small degree of evolution. The photon index increases progressively from $\Gamma_{ph,0} = 0.18$ to 0.28, and the hardness ratio decreases from $H_{R,0} = 2.89$ to 2.17. During this epoch, a soft-to-hard spectral evolution is displayed. The Pearson’s correlation coefficient between the X-ray flux and the photon index is $r_{F,\Gamma_{ph}} = 0.95$ with a p-value of 2×10^{-6} . It indicates that both variables are strongly correlated.

Epoch “I”. During the steep decay, the photon index and the hardness ratio light curves exhibit the strongest evolution. These parameters vary significantly from $\Gamma_{ph,I} = 4.15$ to 1.24, and from $H_{R,I} = 0.59$ to 4.66, respectively. The maximum and minimum photon index corresponds to the maximum and minimum values of the light curve. Similarly, the maximum and minimum hardness ratio corresponds to the maximum and one of the minimum values of the light curve. During this epoch it is shown a soft-to-hard spectral evolution. Using the ROOT software package (Brun and Rademakers 1997), we successfully fit the photon index and hardness ratio as $\Gamma_{ph,I} \propto t^{-0.75 \pm 0.06}$ ($\chi^2/ndf = 0.96$) and $H_{R,I} \propto t^{1.36 \pm 0.19}$ (0.95), respectively. The Pearson’s correlation coefficient between the flux and the photon index is $r_{F,\Gamma_{ph}} = 0.77$ with a p-value of 3×10^{-7} . It indicates a strong correlation between both variables.

Epoch “II” During this epoch, the photon index and the hardness ratio evolve rapidly among two maximum and minimum values. First, the photon index and the hardness ratio vary from $\Gamma_{ph,II} = 1.34$ to 2.32, and from $H_{R,II} = 3.05$ to 1.79, respectively. Once the X-ray flux at 1 keV and 10 keV begins decreasing and increasing, respectively, the photon index and the hardness ratio have a small decrease and increase, respectively, and then keep constant around ≈ 2 . At the end of interval, the photon index and the hardness ratio have a small increase and decrease, respectively, and then these parameters evolve strongly from $\Gamma_{ph,II} = 2.61$ to 1.31, and from $H_{R,II} = 4.34$ to 1.45, respectively.

Epoch “III” During the X-ray flare, the photon index and the hardness ratio displayed random fluctuation around ≈ 3 and ≈ 2.5 , respectively.

Epoch “IV” During the canonical normal decay, a very moderate spectral softening is observed.

3. INTERPRETATION AND MODELLING OF THE MULTI-WAVELENGTH OBSERVATIONS

3.1. Light curves from energy injection by a millisecond magnetar

The energy reservoir of a millisecond magnetar is the total rotation energy which is given by

$$E = \frac{1}{2} I \Omega^2 \approx 2.6 \times 10^{52} \text{ erg } M_{ns,1.4}^{\frac{3}{2}} P_{-3}^{-2}, \quad (1)$$

where P is the spin period associated to an angular frequency $\Omega = 2\pi/P$ and $I \simeq 1.3 \times 10^{45} M_{ns,1.4}^{\frac{3}{2}} \text{ g cm}^2$ (Latimer and Schutz 2005) is the NS moment of inertia with $M_{ns} = 1.4 M_{\odot}$ the NS mass.

CC-SNe are usually expected to leave a fraction of the stellar progenitor bound to NS following the SN explosion. This fraction of material will begin to rotate into an accretion disk and to fall-back over a long period of time (Chevalier 1989; Woosley and Heger 2012; Quataert and Kasen 2012). For

¹⁰ An additional epoch associated to an X-ray flare observed at 10 keV within a timescale of $\sim 10^6$ s could be considered.

¹¹ https://www.swift.ac.uk/xrt_live_cat/00922968/

simplicity, we consider a fall-back accretion rate given by (Metzger et al. 2018)

$$\dot{M} \simeq \frac{2}{3} \frac{M_{\text{fb}}}{t_{\text{fb}}} \begin{cases} 1 & t \ll t_{\text{fb}}, \\ \left(\frac{t}{t_{\text{fb}}}\right)^{-\frac{5}{3}} & t_{\text{fb}} \ll t, \end{cases} \quad (2)$$

where M_{fb} is the accreting mass over a characteristic fall-back time t_{fb} . The dynamics of the magnetar with fall-back accretion depends on the Alfvén (r_m), co-rotation (r_c) and the light cylinder (r_{lc}) radii, which are

$$\begin{aligned} r_m &\simeq 2.2 \times 10^6 \text{ cm } M_{\text{ns},1.4}^{-\frac{1}{2}} \dot{M}_{-2}^{-\frac{2}{7}} B_{15}^{\frac{4}{7}} R_{\text{ns},6.1}^{\frac{12}{7}}, \\ r_c &\simeq 1.7 \times 10^6 \text{ cm } M_{\text{ns},1.4}^{\frac{1}{3}} P_{-3}^{\frac{2}{3}}, \\ r_{\text{lc}} &\simeq 4.8 \times 10^6 \text{ cm } P_{-3}, \end{aligned} \quad (3)$$

respectively, and the spin evolution given by the differential equation (Piro and Ott 2011)

$$I \frac{d\Omega}{dt} = -N_{\text{dip}} + N_{\text{acc}}, \quad (4)$$

with $R_{\text{ns}} \simeq 1.2 \times 10^6 \text{ cm } R_{\text{ns},6.1}$ the NS radius and B the strength of the dipole magnetic field. The terms N_{dip} and N_{acc} are the spin-down torques from the dipole emission and accretion, respectively. For $r_m \gtrsim R_{\text{ns}}$, these torques are (Parfrey et al. 2016)

$$N_{\text{dip}} \simeq \begin{cases} \frac{\mu^2 \Omega^3}{c^3} \frac{r_{\text{lc}}^2}{r_m^2} & r_m \lesssim r_{\text{lc}}, \\ \frac{\mu^2 \Omega^3}{c^3} & r_{\text{lc}} \lesssim r_m, \end{cases} \quad (5)$$

and

$$N_{\text{acc}} = \dot{M} (G M_{\text{ns}} r_m)^{\frac{1}{2}} \left[1 - \left(\frac{r_m}{r_c} \right)^{\frac{3}{2}} \right], \quad (6)$$

where $\mu = BR_{\text{ns}}^3$ is the magnetic moment and G is the gravitational constant. In the most general case, the spin-down luminosity can be estimated as $L_{\text{sd}} = \Omega(N_{\text{dip}} - N_{\text{acc}})$.

The magnetar would accrete depending on the location of the Alfvén relative to the co-rotation radius. For $r_m \lesssim r_c$, the magnetar will accrete, otherwise, the system could enter in the propeller regime (e.g., see Campana et al. 1998). The spin period that delineates both regimes, and also happens to be the steady state evolution of the system is given for the condition $r_m = r_c$. In this case, the spin period in equilibrium becomes

$$P_{\text{eq}} \simeq 1.5 \times 10^{-3} \text{ s } B_{15}^{\frac{6}{7}} R_{\text{ns},6.1}^{\frac{18}{7}} M_{\text{ns},1.4}^{-\frac{5}{7}} \dot{M}_{-2}^{-\frac{3}{7}}, \quad (7)$$

which is reached during a time interval given by $I\Omega_{\text{eq}}/\dot{M}(G M_{\text{ns}} r_m)^{\frac{1}{2}}$ with $\Omega_{\text{eq}} = 2\pi/P_{\text{eq}}$.

3.1.1. GRB prompt emission and the magnetization parameter

The prompt emission in the Poynting-flux-dominated regime will be generated by the magnetic reconnections which could or not induce internal shell collisions. In both cases, the magnetization parameter plays an important role. In some magnetic dissipation models, the magnetization parameter is expected to be similar to the bulk Lorentz factor and lie in the range of $100 \lesssim \sigma \lesssim 3000$ (Liang et al. 2010; Ghirlanda et al. 2012; Beniamini and Giannios 2017).

Irrespective the model, the magnetization parameter is defined by

$$\sigma = \frac{L_j}{\dot{M}_j c^2}, \quad (8)$$

where $L_j = L_{\text{sd}}$ represents the spin-down luminosity (Buciantini et al. 2009) and \dot{M}_j is the rate at which the baryon loading is ejected from the NS surface. In the case of the a weakly-magnetized wind, it can be written as

$$\dot{M}_j \simeq \dot{M}_\nu f_{\text{cent}} \begin{cases} \frac{R_{\text{ns}}}{2 r_m} & r_m \lesssim r_{\text{lc}} \\ \frac{R_{\text{ns}}}{2 r_m} & r_{\text{lc}} \lesssim r_m, \end{cases} \quad (9)$$

with $\dot{M}_\nu = \dot{M}_{\nu,\text{ob}}(t) + \dot{M}_{\nu,\text{acc}}(t)$, $f_{\text{cent}} = e^{(\frac{P}{P_{\text{eq}}})^{\frac{3}{2}}}$ and $P_c \simeq 2.7 R_{\text{ns}}^{\frac{1}{2}} r_m^{-\frac{1}{2}} M_{1.4}^{-\frac{1}{2}}$. The terms $\dot{M}_{\nu,\text{ob}}(t)$ and \dot{M}_{acc} are associated with the mass loss rate due to different sources of neutrinos. The term $\dot{M}_{\nu,\text{ob}}(t)$ defined by (Metzger et al. 2011)

$$\dot{M}_{\nu,\text{ob}}(t) = 3 \times 10^{-4} \left(1 + \frac{t}{t_{\text{kh}}}\right)^{-\frac{5}{2}} e^{-\frac{t}{t_{\text{thin}}}} M_\odot \text{ s}^{-1}, \quad (10)$$

is due to the neutrino ablation, and

$$\dot{M}_{\text{acc}}(t) = 1.2 \times 10^{-5} M_{1.4} \dot{M}_{-2}^{\frac{5}{3}} M_\odot \text{ s}^{-1}, \quad (11)$$

is due to the accretion (Piro and Ott 2011). The cooling timescale $t_{\text{kh}} \approx 2 \text{ s}$ corresponds to Kelvin-Helmholtz and $t_{\text{thin}} \approx (10 - 30) \text{ s}$ to the timescale when NS becomes optically thin to neutrinos (Metzger et al. 2018).

3.2. Synchrotron light curves from external shocks

3.2.1. Light curves from forward shocks

It is a widely accepted that the standard synchrotron emission generated by relativistic electrons accelerated in forward shocks (FSs) can explain the X-ray, optical and radio observations in GRB afterglows. The shape of synchrotron light curves depend on the density profile of the circumburst medium (i.e., uniform-density or wind). The characteristic and cooling spectral breaks and the maximum flux of synchrotron emission evolving in a uniform-density (wind) medium are $\epsilon_{\text{m}}^{\text{syn}} \propto \Gamma^4 (t^{-1} \Gamma^2)$, $\epsilon_{\text{c}}^{\text{syn}} \propto t^{-2} \Gamma^{-4} (t \Gamma^2)$ and $F_{\text{max}}^{\text{syn}} \propto t^3 \Gamma^8 (t^0 \Gamma^2)$, respectively. The predicted synchrotron light curves during the early and late afterglow for the thick and thin shell regime are briefly introduced for an electron distribution of Lorentz factor γ_e^{-p} with p is the spectral index (Sari et al. 1998).

3.2.1.1. The early afterglow. — During the early afterglow, before the jet begins to decelerate the bulk Lorentz is constant $\Gamma \propto t^0$ (coasting phase). In this phase, the synchrotron spectral breaks and the maximum flux in the uniform-density (wind) medium are $\epsilon_{\text{m}}^{\text{syn}} \propto t^0 (t^{-1})$, $\epsilon_{\text{c}}^{\text{syn}} \propto t^{-2} (t)$ and $F_{\text{max}} \propto t^3 (t^0)$, respectively. The predicted synchrotron light curves in the uniform-density (wind) medium for the fast- and slow-cooling regime are

$$F_\nu^{\text{syn}} \propto \begin{cases} t^2 (t^{\frac{1}{2}}) \epsilon_\gamma^{-\frac{1}{2}}, & \epsilon_{\text{c}}^{\text{syn}} < \epsilon_\gamma < \epsilon_{\text{m}}^{\text{syn}}, \\ t^2 (t^{\frac{2-p}{2}}) \epsilon_\gamma^{-\frac{p}{2}}, & \epsilon_{\text{m}}^{\text{syn}} < \epsilon_\gamma, \end{cases} \quad (12)$$

and

$$F_\nu^{\text{syn}} \propto \begin{cases} t^3 (t^{\frac{1-p}{2}}) \epsilon_\gamma^{-\frac{p-1}{2}}, & \epsilon_{\text{m}}^{\text{syn}} < \epsilon_\gamma < \epsilon_{\text{c}}^{\text{syn}}, \\ t^2 (t^{\frac{2-p}{2}}) \epsilon_\gamma^{-\frac{p}{2}}, & \epsilon_{\text{c}}^{\text{syn}} < \epsilon_\gamma, \end{cases} \quad (13)$$

respectively. The synchrotron spectral breaks are reported in Sari and Piran (1999a,b).

3.2.1.2. *The thick-shell regime.* — During this regime, this shock is relativistic early. The bulk Lorentz factor and therefore the synchrotron spectral breaks and the maximum flux in the uniform-density (wind) medium evolves as $\Gamma \propto t^{-\frac{1}{4}}(t^0)$, $\epsilon_m^{\text{syn}} \propto t^{-1}(t^{-1})$, $\epsilon_c^{\text{syn}} \propto t^{-1}(t)$ and $F_{\text{max}} \propto t(t^0)$, respectively. The predicted synchrotron light curves in the uniform-density (wind) medium for the fast- and slow-cooling regime are

$$F_{\nu}^{\text{syn}} \propto \begin{cases} t^{\frac{1}{2}}(t^{\frac{1}{2}})\epsilon_{\gamma}^{-\frac{1}{2}}, & \epsilon_c^{\text{syn}} < \epsilon_{\gamma} < \epsilon_m^{\text{syn}}, \\ t^{-\frac{p-2}{2}}(t^{-\frac{p-2}{2}})\epsilon_{\gamma}^{-\frac{p}{2}}, & \epsilon_m^{\text{syn}} < \epsilon_{\gamma}, \end{cases} \quad (14)$$

and

$$F_{\nu}^{\text{syn}} \propto \begin{cases} t^{-\frac{p-3}{2}}(t^{-\frac{p-1}{2}})\epsilon_{\gamma}^{-\frac{p-1}{2}}, & \epsilon_m^{\text{syn}} < \epsilon_{\gamma} < \epsilon_c^{\text{syn}}, \\ t^{-\frac{p-2}{2}}(t^{-\frac{p-2}{2}})\epsilon_{\gamma}^{-\frac{p}{2}}, & \epsilon_c^{\text{syn}} < \epsilon_{\gamma}, \end{cases} \quad (15)$$

respectively. The synchrotron spectral breaks are reported in [Gao et al. \(2013\)](#); [Yi et al. \(2013\)](#).

3.2.1.3. *The deceleration phase (the thin-shell regime).* — In the deceleration phase, the bulk Lorentz in the uniform-density (wind) medium evolves as $\Gamma \propto t^{-\frac{3}{8}}(t^{-\frac{1}{4}})$. The synchrotron spectral breaks and the maximum flux in the uniform-density (wind) medium become $\epsilon_m^{\text{syn}} \propto t^{-3/2}(t^{-3/2})$, $\epsilon_c^{\text{syn}} \propto t^{-\frac{1}{2}}(t^{\frac{1}{2}})$ and $F_{\text{max}} \propto t^0(t)$, respectively. The predicted synchrotron light curves in the uniform-density (wind) medium for the fast- and slow-cooling regime are

$$F_{\nu}^{\text{syn}} \propto \begin{cases} t^{-\frac{1}{4}}(t^{-\frac{1}{4}})\epsilon_{\gamma}^{-\frac{1}{2}}, & \epsilon_c^{\text{syn}} < \epsilon_{\gamma} < \epsilon_m^{\text{syn}}, \\ t^{-\frac{3p-2}{4}}(t^{-\frac{3p-2}{4}})\epsilon_{\gamma}^{-\frac{p}{2}}, & \epsilon_m^{\text{syn}} < \epsilon_{\gamma}, \end{cases} \quad (16)$$

and

$$F_{\nu}^{\text{syn}} \propto \begin{cases} t^{-\frac{3p-3}{4}}(t^{-\frac{3p-1}{4}})\epsilon_{\gamma}^{-\frac{p-1}{2}}, & \epsilon_m^{\text{syn}} < \epsilon_{\gamma} < \epsilon_c^{\text{syn}}, \\ t^{-\frac{3p-2}{4}}(t^{-\frac{3p-2}{4}})\epsilon_{\gamma}^{-\frac{p}{2}}, & \epsilon_c^{\text{syn}} < \epsilon_{\gamma}, \end{cases} \quad (17)$$

respectively. The synchrotron spectral breaks are reported in [Sari et al. \(1998\)](#); [Kobayashi \(2000\)](#); [Chevalier and Li \(2000\)](#); [Panaitescu and Kumar \(2000\)](#).

3.2.2. Light curves from reverse shocks

In order to analyze the X-ray/optical flare, the predicted synchrotron light curves in the reverse shock (RS) region are given before and after the shock crossing time

3.2.2.1. *Before the shock crossing time.* — The synchrotron light curves evolving in the uniform-density (wind) medium for the fast and slow-cooling regime are

$$F_{\nu,r}^{\text{syn}} \propto \begin{cases} t^{\frac{1}{2}}(t^0)\epsilon_{\gamma}^{-\frac{1}{2}}, & \epsilon_{c,r}^{\text{syn}} < \epsilon_{\gamma} < \epsilon_{m,r}^{\text{syn}}, \\ t^{\frac{6p-5}{2}}(t^{\frac{p-1}{2}})\epsilon_{\gamma}^{-\frac{p}{2}}, & \epsilon_{m,r}^{\text{syn}} < \epsilon_{\gamma}, \end{cases} \quad (18)$$

and

$$F_{\nu,r}^{\text{syn}} \propto \begin{cases} t^{\frac{6p-3}{2}}(t^{\frac{p-2}{2}})\epsilon_{\gamma}^{-\frac{p-1}{2}}, & \epsilon_{m,r}^{\text{syn}} < \epsilon_{\gamma} < \epsilon_{c,r}^{\text{syn}}, \\ t^{\frac{6p-5}{2}}(t^{\frac{p-1}{2}})\epsilon_{\gamma}^{-\frac{p}{2}}, & \epsilon_{c,r}^{\text{syn}} < \epsilon_{\gamma}, \end{cases} \quad (19)$$

respectively. The sub-index “r” corresponds to the spectral breaks and observed flux in the reverse shocks. The synchrotron spectral breaks are reported in [Kobayashi \(2000\)](#); [Chevalier and Li \(2000\)](#); [Panaitescu and Kumar \(2000\)](#); [Fraija et al. \(2019c\)](#).

3.2.2.2. *After the shock crossing time.* — The synchrotron light curves evolving in the uniform-density (wind) for the fast and slow-cooling regime are

$$F_{\nu,r}^{\text{syn}} \propto \begin{cases} t^{-\frac{32}{35}}(t^{-\frac{11}{14}})\epsilon_{\gamma}^{-\frac{1}{2}}, & \epsilon_{c,r}^{\text{syn}} < \epsilon_{\gamma} < \epsilon_{m,r}^{\text{syn}}, \\ t^{-\frac{27p+5}{35}}(t^{-\frac{2-13p}{14}})\epsilon_{\gamma}^{-\frac{p}{2}}, & \epsilon_{m,r}^{\text{syn}} < \epsilon_{\gamma}, \end{cases} \quad (20)$$

and

$$F_{\nu,r}^{\text{syn}} \propto \begin{cases} t^{-\frac{27p+7}{35}}(t^{-\frac{39p+7}{42}})\epsilon_{\gamma}^{-\frac{p-1}{2}}, & \epsilon_{m,r}^{\text{syn}} < \epsilon_{\gamma} < \epsilon_{c,r}^{\text{syn}}, \\ t^{-\frac{27p+5}{35}}(t^{-\frac{2-13p}{14}})\epsilon_{\gamma}^{-\frac{p}{2}}, & \epsilon_{c,r}^{\text{syn}} < \epsilon_{\gamma}, \end{cases} \quad (21)$$

respectively. Again, the synchrotron spectral breaks are reported in [Kobayashi \(2000\)](#); [Chevalier and Li \(2000\)](#); [Panaitescu and Kumar \(2000\)](#); [Fraija et al. \(2016a\)](#).

3.3. Theoretical Interpretation

3.3.1. The initial gamma-ray pulse and the X-ray precursor

The initial gamma-ray pulse is fitted with an exponential function $\propto \exp(-\frac{t}{\tau_2})$ with $\tau_2 = 0.39 \pm 0.10$ s. In order to interpret these observations, we discuss different scenarios such as an expanding cocoon, an external shock emission, a high-latitude emission by a relativistic shock breakout and the spin-down magnetar.

3.3.1.1. *Expanding Cocoon.* — [Pe’er et al. \(2006\)](#) showed that fluxes varying as $t^{-\alpha}$ with $\alpha \approx 2.5 - 4$ could be interpreted as the thermal emission from the expanding cocoon once the jet has broken through the stellar envelope. In a multi-color BB scenario ([Ryde and Pe’er 2009](#)), photons emitted from different angles and with distinct Doppler boosting, the flux of a thermal spectrum decays as $\propto t^{-2}$. Given that the thermal emission is not observed in the GBM and the BAT data,¹² we discard the idea that the X-ray precursor and initial gamma-ray pulse could have been produced from an expanding cocoon.

3.3.1.2. *External shocks.* — [O’Brien et al. \(2006\)](#) presented the early X-ray observations for 40 bursts using Swift data from BAT and XRT instruments. Authors proposed that the X-ray light curves could be interpreted as a superposition of the prompt emission and the afterglow. [Huang et al. \(2018\)](#) systematically investigated single-pulse GRBs in the Swift era. Authors found that the prompt emission and the afterglow in a small fraction of bursts originated from external shocks. Some authors have suggested that a single smooth peak or temporally separated peaks during the prompt emission are likely created by external shocks ([McMahon et al. 2004](#); [Dermer and Mitman 2004](#); [Burgess et al. 2016](#); [Golkhou and Butler 2014](#)). Concerning GRB 190829A, the initial gamma-ray pulse fits much better with a Band than the CPL function and the BAT observations with a PL than a CPL for a photon index of $\Gamma_x = \beta_x + 1 = 3.23$. Although the peak energy evolves as $\propto t^{-\frac{3}{2}}$, similar to the synchrotron FS model in the fast cooling regime when the outflow decelerates by a uniform-density or wind medium, the atypical value of the spectral index $p \approx 5.5$ disagrees with this model ($\beta_x = \frac{p-1}{2}$; [Sari et al. 1998](#)). Therefore, we discard that the X-ray precursor and initial gamma-ray pulse could have been generated by FSs. This result is reaffirmed through the analysis of the GRB tail emission (see subsection 4.3) that indicates the prompt emission and the afterglow originate from different components.

¹² For BAT analysis see: https://gcn.gsfc.nasa.gov/notices_s/922968/BA/

3.3.1.3. *High-latitude emission by a relativistic shock breakout.*— Nakar and Sari (2012) computed the luminosity, the light curve and the spectrum generated by a relativistic breakout, then the planar phase and finally, the spherical phase. They found that spherical relativistic breakouts produce a gamma-ray flash with an energy, temperature, duration and Lorentz factor well defined and related each other. In addition, they reported that the predicted flux between the planar and spherical relativistic phase evolves as $\propto t^{-2}$, due to the curvature effect (delayed photons arriving from high latitudes). Although the evolution of the flux due to the curvature effect is equal to the initial gamma-ray pulse a thermal emission is not observed in the GBM and BAT data. Therefore, we discard that the early X-ray observations and the initial gamma-ray pulse can be interpreted by this mechanism.

3.3.1.4. *Spin-down Magnetar.*— The initial gamma-ray pulse and the X-ray precursor are consistent with the light curve of the spin-down magnetar for a timescale much less than a characteristic fall-back time. Considering the case of $r_c \ll r_m$, the equation (4) becomes

$$\frac{d\Omega}{dt} + \left(\frac{\mu^2}{c^3 I r_m^2} + \frac{\dot{M} r_m^2}{I} \right) \Omega = 0, \quad (22)$$

which has as solution $\Omega \propto \exp(-\frac{t}{2t_{\text{sd}}})$ where the characteristic timescale is $t_{\text{sd}} = \frac{1}{2} \left(\frac{\mu^2}{c^3 I r_m^2} + \frac{\dot{M} r_m^2}{I} \right)^{-1}$. From the evolution of angular frequency, the spin-down luminosity becomes

$$L_{\text{sd}} \propto \exp(-\frac{t}{t_{\text{sd}}}), \quad (23)$$

which has a similar profile to the best-fit curve found for these observations. Considering the typical values $B = 10^{16}$ G, $P = 10^{-3}$ s and $\dot{M} = 10^{-2} M_{\odot} s^{-1}$, the characteristic timescale is $t_{\text{sd}} \approx 2.25$ s. The eq. 24 agrees with the best-fit curve of the initial gamma-ray pulse and the X-ray precursor.

3.3.2. The “plateau” phase

The X-ray light curve at 1 keV is described by a PL with spectral index 0.06 ± 0.05 that is consistent with a “plateau” phase. In order to interpret the “plateau” phase, we discuss different scenarios such as the PL velocity distribution, the external shock emission and the spin-down magnetar.

3.3.2.1. *A power-law velocity distribution.*— In this scenario the outflow is segmented in several mini-shells each one of them with different velocities. The equivalent kinetic energy of the outflow is associated with a power-law velocity distribution given by $E \propto \Gamma^{-\alpha_{\Gamma}}$ (Tan et al. 2001). The bulk Lorentz factor in a uniform-density (wind) medium evolves as $\Gamma \propto t^{-\frac{3}{\alpha_{\Gamma}+8}} (t^{-\frac{1}{\alpha_{\Gamma}+4}})$ and the predicted flux generated by synchrotron emission evolves as $F_{\nu} \propto t^{\frac{3(\alpha_{\Gamma}-2p+2)}{\alpha_{\Gamma}+8}} (t^{\frac{\alpha_{\Gamma}-6p+2-\alpha_{\Gamma}p}{2(\alpha_{\Gamma}+4)}})$ for $\epsilon_m^{\text{syn}} < \epsilon_{\gamma} < \epsilon_c^{\text{syn}}$ and $F_{\nu} \propto t^{\frac{2(\alpha_{\Gamma}-3p+2)}{\alpha_{\Gamma}+8}} (t^{\frac{2\alpha_{\Gamma}-6p+4-\alpha_{\Gamma}p}{2(\alpha_{\Gamma}+4)}})$ for $\epsilon_c^{\text{syn}} < \epsilon_{\gamma}$ (e.g, see Sari and Mészáros 2000; Zhang et al. 2006; Barniol Duran et al. 2015; Fraija et al. 2019d). In order to reproduce the “plateau” phase, an atypical value of $p \approx 4.0(1.0)$ has to be required for the uniform-density (wind) medium. This is very far from expectations from particle acceleration.

3.3.2.2. *Synchrotron FS emission.*— In this scenario, the “plateau” phase is interpreted as synchrotron FS emission during the thick-shell regime (before the significant deceleration begins). From eqs. 14 and 15 can be seen that the synchrotron FS model evolving in a uniform-density medium can describe these observations for $p = 3.2 \pm 0.2$ ($F_{\nu} \propto t^{0.1 \pm 0.1}$; $\epsilon_m^{\text{syn}} < \epsilon_{\gamma} < \epsilon_c^{\text{syn}}$), $p = 2.1 \pm 0.2$ ($F_{\nu} \propto t^{0.05 \pm 0.10}$; $\epsilon_c^{\text{syn}} < \epsilon_{\gamma}$) and in the wind medium for $p = 1.3 \pm 0.2$ ($F_{\nu} \propto t^{0.1 \pm 0.1}$; $\epsilon_m^{\text{syn}} < \epsilon_{\gamma} < \epsilon_c^{\text{syn}}$). Due to the atypical value required for the wind medium, again we discard it.

For an spectral index of $p = 3.2 \pm 0.2$, the X-ray and optical light curves would evolve in the same PL segment and for $p = 2.1 \pm 0.2$ these bands would evolve in distinct PL segments. Because the X-ray and optical light curves are normalized at $\epsilon_{\gamma}=1$ keV and $\sim (1-3)$ eV, respectively, the predicted optical flux must be much larger than the X-ray flux ($F_{\nu,\text{opt}}/F_{\nu,\text{X}} \gg 1$), for typical values of parameters. However, during this phase the observed fluxes in the White and U bands are less than the observed X-ray flux. Therefore, we discard the synchrotron FS emission as origin of the “plateau” phase.

3.3.2.3. *Spin-down Magnetar.*— Once the system reaches the equilibrium ($r_c = r_m$), the accretion term is zero ($N_{\text{acc}}(\Omega_{\text{eq}}) = 0$), and therefore the spin-down luminosity becomes $L_{\text{sd}} = \Omega N_{\text{dip}}$. From eqs. (5) and (2), the spin-down luminosity is in the form

$$L_{\text{sd}} \simeq \frac{\mu^2 \Omega_{\text{eq}}^4 r_{\text{lc}}^2 (\Omega_{\text{eq}})}{c^3 r_c^2} \propto \begin{cases} t^0 & t \ll t_{\text{fb}}, \\ t^{-\frac{50}{21}} & t_{\text{fb}} \ll t, \end{cases} \quad (24)$$

which for $t \ll t_{\text{fb}}$ is consistent with the best-fit curve during this phase. It is worth noting that the best-fit value of 0.573 ± 0.013 reported by the Swift analysis¹³ during the time interval $\sim (10^2 - 10^5)$ s would agree with the light curve given by eq. (24) during the transition around t_{fb} .

Other mechanisms such as a photospheric component from a moderate outflow injected after the prompt emission (Beniamini and Mochkovitch 2017) and viewing of bursts very slightly off-axis (Beniamini et al. 2020) have been recently proposed to interpret the “plateau” phase. However, a photospheric component was not clearly observed in this burst and the E_{peak} and E_{iso} relation indicates that this burst was on-axis (see subsection 4.4), so these mechanism are discarded.

3.3.3. A normal decay phase

After the break time of $1.4_{-0.15}^{+0.17} \times 10^5$ s, the best fit of the X-ray observations reported was $\alpha_{\text{X,IV}} = 1.24 \pm 0.04$.¹⁴ Before the break time, a temporal index of $\alpha_{\text{X,IV}} = 1.05 \pm 0.02$ was obtained. These observations are consistent with the synchrotron FS model evolving in the slow-cooling regime and in a uniform-density medium for $p \approx 2.3$. During this phase, the hardness ratio light curve shows a very moderate spectral softening.

Spectral analysis at 1.8×10^4 s indicates that the X-ray and optical observations evolve in the same PL segment

¹³ https://www.swift.ac.uk/xrt_live_cat/00922968/1_breaks.png

¹⁴ https://www.swift.ac.uk/xrt_live_cat/00922968/

with spectral slope of $\beta_{X,O} = 0.47 \pm 0.09$. This value is consistent with the PL segment of the slow-cooling regime $\epsilon_m^{\text{syn}} < \epsilon_\gamma < \epsilon_c^{\text{syn}}$ for $p = 1.98 \pm 0.05$. Otherwise, an atypical value of p is obtained where X-ray and optical observations would evolve in distinct PL segments.

Taking into account the temporal and spectral analysis (the closure relations given by eq. 17), this phase is consistent with synchrotron FS model that evolves during the deceleration phase in a uniform-density medium for $p = 2.15 \pm 0.17$. The value of p is consistent with the range of values typically for GRB afterglows (Kumar and Zhang 2015).

3.3.4. The X-ray and optical flares

The X-ray and optical flares occurred simultaneously peaking at $\sim 1.4 \times 10^3$ s with rising and falling slopes of ≈ -3 and ≈ 1 , respectively. In what follows we discuss the late central-engine activity, the neutron signature and the synchrotron emission from external shocks as possible scenarios.

3.3.4.1. Late central-engine activity. — In the fireball model, faster shells in an emitting region of the jet interact with slower ones. If the comoving magnetic field in the emitting region is random or transverse, the flux would evolve as $t^{-\alpha}$ with $\alpha = 2(p+1)$ or $\frac{2-3p}{2}$, respectively, if the synchrotron emission evolves in the fast-cooling regime for $\beta = \frac{p}{2}$, and $\alpha = 2p$ or $\frac{1-3p}{2}$, respectively, in the slow cooling regime for $\beta = \frac{1-p}{2}$. Given the best-fit values of the falling slopes of the X-ray and optical flares (see Tables 4 and 3), an atypical value of $p < 1$ would have to be required to reproduce these flares. As the falling slopes are less than < 2 , these cannot be interpreted in the context of high-latitude emission. Considering the simultaneity of the X-ray and optical flares and that the best-fit values of the timescale lie in the range of 0.68 - 0.9 and, internal shocks created by late central-engine activity cannot reproduce the features of these flares. It is important to highlight that the photon index and the hardness ratio displayed random fluctuations around ≈ 3 and ≈ 2.5 , respectively, different to the behavior during the flaring activity (see section 2.2.4.1).

3.3.4.2. Neutron Signature. — A relevant process that could describe the X-ray and optical flares is associated with the presence of neutrons in the outflow (Derishev et al. 1999; Fraija 2014). It occurs as neutrons and ions are fully decoupled; neutrons create a leading front and ions start to slow down. Then, neutrons decay in products that interact with the slow-moving ions and produce a re-brightening in the early afterglow (Beloborodov 2003). Fan and Wei (2005) introduced an analytic formalism to derive the light curves and spectrum. Authors showed that the resulting light-curve initially increases fast, then there comes a flat phase the duration of the burst and finally, it drops sharply. Although, the light curve by this scenario has a similar profile to those displayed in GRB 190829A, this occurs at early times ($\sim T_{90}$). Given that the X-ray and optical flares peak at $\sim 1.4 \times 10^3$ s, we conclude that neutron-proton decoupling cannot describe these flares exhibited in GRB 190829A.

3.3.4.3. Synchrotron RS emission. — Synchrotron emission from RSs are usually required to describe X-ray and optical flares (Kobayashi 2000; Fraija et al. 2016b, 2017b; Fraija and Veres 2018). From eqs. (18) - (21) can be seen that before and after

the shock crossing time, the synchrotron RS model evolving in slow-cooling regime and uniform-density medium could describe the temporal and spectral observations but for an atypical value of $p \approx 1.3 \pm 0.2$. Similarly, the fact that the soft X-ray and optical fluxes are simultaneous during more than $\sim 10^4$ s with similar slopes disfavor the synchrotron RS scenario. It is worth noting that the predicted synchrotron light curves evolving in a wind medium cannot explain the rising slopes.

3.3.4.4. Synchrotron FS emission. — At early times, the optical and X-ray light curves show bright simultaneous flares peaking at $\sim 1.4 \times 10^3$ s with variability timescales in the range of $\Delta t/t \approx 0.68 - 0.9$. Tables 3 and 4 show that during the time interval $\sim (0.65 - 1.4) \times 10^3$ s, the X-ray and optical fluxes increase as $t^{-\alpha}$ with slopes of ≈ -3 , reaching a maximum flux at $\sim 1.4 \times 10^3$ s. The closure relations during the early afterglow/coasting phase (eqs. 12 and 13) indicate that the synchrotron FS model is the slow-cooling regime ($\epsilon_m^{\text{syn}} < \epsilon_\gamma < \epsilon_c^{\text{syn}}$) and evolving in a uniform-density medium could describe these observations. It is worth noting that the predicted synchrotron light curves evolving in a wind medium cannot reproduce the rising slopes for any value of the electron spectral index. In the deceleration phase, the predicted synchrotron light curves decrease as $t^{-\alpha}$ with $\alpha \approx 1$ for $p=2.3$ which is consistent once the X-ray and optical fluxes begin to decrease (see eqs. 16 and 17). On the other hand, spectral analysis at 6×10^3 s and 1.8×10^4 s indicate that the X-ray and optical observations evolve in the same PL segment with a spectral slope of $\beta_{X,O} = 0.48 \pm 0.05$ and 0.47 ± 0.09 , respectively. These values are consistent with the PL segment of slow-cooling regime $\epsilon_m^{\text{syn}} < \epsilon_\gamma < \epsilon_c^{\text{syn}}$ for $p \approx 2$.

Finally, the temporal and spectral analysis indicates that the X-ray and optical flares can be theoretically described as synchrotron FS emission for $p \approx 2.15 \pm 0.17$.

It is worth noting that photospheric emission from moderate Lorentz factor material that is emitted at the same time as the material producing the prompt leads to much weaker flares in the optical compared to X-rays, so it may not be appropriate here (Beniamini and Kumar 2016).

3.4. Modelling the multi-wavelength light curves

The spin-down luminosity can be converted into isotropic X-ray flux through the efficiency in converting its spin-down energy to radiation (η_x) and the beaming factor of the magnetar wind ($f_b = 1 - \cos \theta_j$). The X-ray luminosity can be written as

$$L_x = \eta_x f_b^{-1} L_{\text{sd}}. \quad (25)$$

Similarly, considering the typical energy range of Swift XRT and the photon spectral index for GRB 190829A, the X-ray luminosity could be converted to X-ray flux at 1 keV using the relationship $F_x \simeq \frac{L_x}{4\pi d_z^2}$. The term d_z corresponds to the luminosity distance which is estimated using the values of the Hubble constant as $H_0 = (67.4 \pm 0.5) \text{ km s}^{-1} \text{ Mpc}^{-1}$ and the matter density parameter as $\Omega_m = 0.315 \pm 0.007$ (Planck Collaboration et al. 2018).

The upper panels in Figure 3 show the X-ray (BAT and XRT) light curve at (0.3 -10) keV energy range with the best-fit curve given by the spin-down magnetar (left) and

the evolution of the Alfvén (r_m), co-rotation (r_c) and the light cylinder (r_{lc}) radii (right). Swift data in the small box included in the upper left-hand panel is reported at 10 keV. The fit was done using the MINUIT algorithm (James and Roos 1975) via the `iminuit`¹⁵ Python interface. We use the interpolation of the solution using the `interp1d` function from the `scipy.interpolate` Python object and the χ^2 regression function with the `Chi2Regression` object from the `probit` Python interface. A set of initial values are placed in order to minimize the function with the `iminuit` interface and the `migrad` optimiser. We assume a fall-back mass of $M_{fb} = 0.8M_\odot$ (Metzger et al. 2018), $\theta_j = 8^\circ$ (see analysis in section 4.3) and $\eta_x = 0.1$ (Bernardini et al. 2013). The best-fit values of the magnetic field, the spin period and the fall-back timescale are reported in Table 7. This panel shows the evolution of the magnetization parameter (below). This parameter lies at two separate time intervals in the range of $100 \lesssim \sigma \lesssim 3000$; before a few seconds and larger than ~ 80 s. The small box shows that evolution of the magnetization parameter agrees with the flaring activity at (15–50) keV energy range. During the early X-ray observations the extracted rotational energy is 4.18×10^{50} erg and during the “plateau” phase is 2.93×10^{47} erg. Comparing the extracted rotational energy associated to the precursor with the isotropic-equivalent energy (see Table 1), we can estimate an efficiency of $(21.7 \pm 1.13)\%$. The upper right-hand panel shows that the spin period reaches its equilibrium at ~ 10 s (on a timescale of $\sim 10^{-3} t_{fb}$). During the first seconds, the light cylinder radius is less than Alfvén radius, so the spin-down luminosity is similar to the isolated magnetar. The system lies in the propeller regime so that the angular momentum losses decrease the total rotational energy.

The lower panel shows the multi-wavelength light curves of GRB 190829A with the best-fit curves given by the spin-down magnetar and the synchrotron FS model. The UVOT data is exhibited at the V band. The quantities observed for GRB 190829A such as the redshift $z = 0.078$, the isotropic-equivalent energy 2.967×10^{50} erg and the spectral index $\Gamma_x = 2.2$ ¹⁶ are used. The solid line in blue shows the total contribution (the spin-down magnetar and the synchrotron FS model, see the small box) and in magenta show the synchrotron FS model with the host galaxy contribution. The best-fit values of the uniform-density medium (n), the equivalent-kinetic energy (E), the spectral index (p) and the microphysical parameters given to accelerate electrons (ε_e) and to amplify the magnetic field (ε_B) during the FSs are reported in Table 7. Given the parameters found with our model we can estimate: i) the value of the initial bulk Lorentz factor to be $\Gamma \simeq 34$ which is low for a hGRB and high for a lGRB (Schulze et al. 2014), ii) the deceleration radius at the peak time (1.4×10^3 s) of the afterglow is $R_{dec} \simeq 0.05$ pc, iii) the efficiency to convert the kinetic energy into photons is $\eta_k = 12.4\%$ which is typical for GRB afterglows (Kumar and Zhang 2015; Beniamini et al. 2015) and iv) the spectral break energies are $\epsilon_m^{syn} = 1.9$ eV and $\epsilon_c^{syn} = 0.1$ MeV which indicate that synchrotron model evolves in the slow-cooling regime.

Based on the analysis and modelling of the multi-wavelength

observations, we present a full discussion of GRB 190829A

4. RESULTS AND DISCUSSION

4.1. Non-existence of the thermal emission

Evoking the photosphere, the shock breakout and the cocoon models, the thermal emission is expected during the precursor and the main emission episode. For GRB 190829A, the Band function fits better the GBM data (the initial pulse and the brighter peak) than the BB function, and the PL function fits the BAT data better than the BB function.¹⁷ The non-detection of a clear thermal emission in both the GBM and BAT data indicates that GRB jet outflow might be dotted with a significant fraction of magnetic field (Zhang and Pe’er 2009; Gao and Zhang 2015) or the Band function is the result of the reprocessed quasi-thermal emission from kinetic or magnetic dissipation processes near the photosphere (Pe’er et al. 2006; Lazzati and Begelman 2010; Vurm and Beloborodov 2016; Ahlgren et al. 2015; Lundman et al. 2013; Vurm et al. 2011; Veres et al. 2012). In the standard fireball model, the prompt emission is expected to be a superposition of non-thermal and quasi-thermal photosphere components as found in the BATSE (Ryde and Pe’er 2009) and Fermi (Ryde et al. 2010; Guiriec et al. 2015) data. The detection of a single non-thermal emission as well as the evolution of the spectral parameters (see subsection 2.2.1.1) would favor the scenario of a Poynting-flux-dominated outflow (Zhang and Pe’er 2009; Gao and Zhang 2015; Beniamini and Piran 2014).

4.2. The brighter gamma-ray peak

Analysis of the brighter peak indicates that the gamma-ray flux decays as $F_\nu \propto t^{-6.58 \pm 1.26}$. This decay can be interpreted in terms of internal shocks. During these shocks, a large fraction of Poynting flux is converted into kinetic energy and dissipated at larger radii. Taking into consideration the temporal decay index of 6.58 ± 1.26 , a random magnetic field in the emitting region for $p = 3.29 \pm 0.63$ is favored. Similarly, the peak energy evolves as a function of time $\propto t^{-\alpha_{peak}}$ with a temporal index of $\alpha_{peak} \sim 1$ which is consistent with internal shocks (e. g., see Metzger et al. 2011; Beniamini et al. 2017). It is worth noting that the internal shock scenario agrees with the low- and high-energy spectral index $\alpha \approx -1.1$ and $\beta \approx -2.5$, respectively. The value of low-energy spectral index of ~ -1 is consistent with the synchrotron radiation in magnetic dissipation models that require large dissipation radius ($\sim 10^{15}$ cm; Uhm and Zhang 2014; Beniamini and Granot 2016; Beniamini et al. 2018).

4.3. Analysis of the GRB tail emission

The GRB tail emission marks the end of the prompt phase and also the onset of the afterglow (Zhang et al. 2006). This emission reveals whether the prompt emission and the afterglow originate from distinct components or emitting sites. If the prompt emission and the afterglow arise from distinct components or emission sites, an abrupt decay in the flux level should be observed during the transition phase between the prompt emission and the afterglow. Such an abrupt decay which accounts for the delayed photons is associated with the

¹⁵ A python interface to minuit. Accessed: 2018-03-05. <https://github.com/scikit-hep/iminuit>

¹⁶ https://www.swift.ac.uk/xrt_spectra/00922968/

¹⁷ For BAT analysis see: <https://gcn.gsfc.nasa.gov/notices.s/922968/BA/>

high-latitude emission due to the curvature effect. Kumar and Panaitescu (2000) showed that the observed flux associated to high latitudes evolves as $F_\nu \propto t^{-(2+\beta)}$, where β refers to the spectral index of the synchrotron emission, $\beta = \frac{1}{2}$ or $\frac{p}{2}$ for fast- and $\beta = \frac{1-p}{2}$ or $\frac{p}{2}$ for slow-cooling regime. It is worth mentioning that some variations to the curvature effect model including a non-power-law spectrum (Zhang et al. 2009), an anisotropic emission (Beloborodov et al. 2011; Barniol Duran et al. 2016; Beniamini and Granot 2016), a structured jet (Golkhou and Butler 2014), etc., that leads to a different flux evolution during this phase have been proposed.

During the interval $82 \lesssim t \lesssim 215$ s, the X-ray light curve at 1 keV exhibited a fast decay which is difficult to explain by invoking the external shock model. Some authors have argued that central engines cannot die suddenly, and that the observed GRB tails may give account about the dying history of the central engines (Fan and Wei 2005; Barniol Duran and Kumar 2009). Given the best-fit value of the steep decay of the GRB tail emission $\alpha_{X,I} = 3.53 \pm 0.70$ and the strong variation exhibited by the spectral index and the hardness ratio, the X-ray observations in GRB 190829A during this epoch can be interpreted in the context of the high-latitude emission for $p = 3.06 \pm 1.40$ (Kumar and Panaitescu 2000). This value is consistent with the spectral index ($p = 3.29 \pm 0.63$) derived from the brighter gamma-ray peak (see subsection 4.2). The hardness ratio light curve shows a soft-to-hard spectral evolution. As seen in other bursts detected by Swift (Goad et al. 2007), a temporal analysis shows that the photon index and source intensity are highly correlated with the spectrum being harder when brighter. This result clearly indicates that the steep decay observed in the Swift XRT data is related to the prompt emission (Barthelmy et al. 2005; Tagliaferri et al. 2005).

Given the GRB tail emission, the opening angle for a canonical jet can be estimated as

$$\theta_j \approx 8^\circ \left(\frac{1+z}{1.08} \right)^{-\frac{1}{2}} t_{\text{tail},2}^{\frac{1}{2}} R_{\text{cr},14.5}^{-\frac{1}{2}}, \quad (26)$$

where t_{tail} is the duration of the tail and R_{cr} is the curvature radius. Using the opening angle, the initial bulk Lorentz factor is $\Gamma \gtrsim 25 \frac{t_{\text{tail},2}^{\frac{1}{2}}}{\sqrt{1-\cos \theta_j}}$ which is consistent with the value estimated from peak time of the afterglow.

Before and after the GRB tail emission we identify the prompt emission and afterglow, respectively. A rough comparison between the X-ray emission level during the prompt emission and the afterglow could indicate if both emissions originated in the same component (Zhang et al. 2006). Given the low-energy spectral index α_{Band} , the energy peak and the total isotropic energies reported in Table 1, the duration of the burst, the equivalent kinetic energy ($E_k = 10^{52}$ erg), the energy at which the X-rays are reported ($E_X = 1$ keV) and microphysical parameter ($\varepsilon_e \approx 0.1$), the flux ratio is (see, Zhang et al. 2006)

$$\frac{F_{\nu,X}^{\text{PR}}}{F_{\nu,X}^{\text{ag}}} \approx 0.4 \left(\frac{E_{\gamma,\text{iso},51}}{E_{k,52}} \right) \left(\frac{t_2}{T_{90}} \right) \left(\frac{E_{X,1 \text{ keV}}}{E_{\text{pk},10 \text{ keV}}} \right)^{\alpha_{\text{Band}}+2} \varepsilon_{e,-1}^{-1}, \quad (27)$$

which is in stark contrast with the flux ratio ($> 10^4$) observed in GRB 190829A. This result agree with our model where the prompt emission and the afterglow originate from different components.

4.4. $E_{\text{peak}} - E_{\gamma,\text{iso}}$ Relation

Using the derived values of the total isotropic energy $(2.967 \pm 0.032) \times 10^{50}$ erg and the peak energy of the gamma-ray spectrum $E_{\text{peak}} = 11.47 \pm 0.360$ keV, we found that GRB 190829A is consistent with the $E_{\text{peak}} - E_{\gamma,\text{iso}}$ relation (Amati relation; Amati et al. 2002; Amati 2006) as other GRB-SNe associated with millisecond magnetars (Cano et al. 2014). Figure 4 shows the E_{peak} and $E_{\gamma,\text{iso}}$ relation for GRBs detected by Konus-Wind, Swift BAT and the low-, intermediate- and high-IGRB sample within $z \lesssim 0.2$. The best-fit value of the correlation is adapted from D’Elia et al. (2018). The low-, intermediate- and high-IGRBs are obtained from GRB 980425/ SN 1998bw (Galama et al. 1998), GRB 060218/ SN 2006aj (Campana and et al. 2006), GRB 100316D/ SN 2010bh (Cano et al. 2011), GRB 161219B/ SN 2016jca (Cano et al. 2017; Ashall et al. 2019), GRB 171205A/ SN 2017iuk (Izzo et al. 2019), GRB 130702A/ SN 2013dx (D’Elia et al. 2015) and GRB 030329/ SN 2003dh (Hjorth et al. 2003). It worth noting that GRB 190829A follows this relation, indicating that this burst was not off-axis.

5. ANALYSIS AND DISCUSSION OF THE MULTI-GEV PHOTONS

5.1. Synchrotron limit

Given the best-fit parameters (see Table 7), we plot in the left-hand panel in Figure 5 the evolution of the maximum energy photon radiated by the synchrotron FS model in uniform-density medium. In addition, we plot the VHE emission in the range reported by H.E.S.S.. It is shown that the VHE photons cannot be interpreted in the synchrotron FS scenario. Therefore, an additional mechanism should be present during the FSs to explain these multi-GeV photons. However, photons at hundreds of MeVs below the synchrotron limit can be explained in terms of synchrotron FS scenario (Kumar and Barniol Duran 2009).

Synchrotron photons radiated in the FSs can be up-scattered by the same electron population. Here, we use the best-fit parameters reported in Table 7 and the SSC emission during the deceleration phase in a uniform-density medium introduced in Fraija et al. (2019a).

5.2. Synchrotron-self Compton FS model

Once the jet begins decelerating, the intrinsic attenuation due to $\gamma\gamma$ interactions¹⁸ can be estimated by (e.g., see Veddrenne and Atteia 2009)

$$\tau_{\gamma\gamma,\text{in}} \simeq 10^{-1} R_{\text{dec},17} \Gamma_{1.5}^{-1} n_{\gamma,10.7}, \quad (28)$$

where $R_{\text{dec}} = 2.7 \times 10^{17} \text{ cm } n^{-\frac{1}{3}} E_{51.2}^{\frac{1}{3}} \Gamma_{1.5}^{-\frac{2}{3}}$ is the radius at the deceleration phase and $n_\gamma \simeq 5 \times 10^{10} \text{ cm}^{-3} L_{\gamma,49} R_{\text{dec},17}^{-2} \Gamma_{1.5}^{-1} \varepsilon_{\gamma,3}^{-1}$ is the density of the keV-energy photons associated with its photon luminosity. Due to the fact that $\tau_{\gamma\gamma,\text{in}} \ll 1$, the intrinsic attenuation is not considered.

The minimum and the cooling electron Lorentz factors are

$$\gamma_m = 4.3 \times 10^2 \varepsilon_{e,1.1} \Gamma_{1.5},$$

¹⁸ VHE gamma-ray photons can interact with lower-energy photons to produce pairs

$$\gamma_c = 8.4 \times 10^5 \left(\frac{1+z}{1.08} \right) [1 + Y(\gamma_c)]^{-1} \varepsilon_{B,-4}^{-1} n^{-1} \Gamma_{1.5}^{-3} t_3^{-1}, \quad (29)$$

where $Y(\gamma_c)$ corresponds to the Compton parameter of the electrons with Lorentz factor γ_c (Wang et al. 2010). The value of $Y(\gamma_c)$ is given by

$$Y(\gamma_c) = \frac{\eta \varepsilon_e}{\varepsilon_B [1 + Y(\gamma_c)]} \begin{cases} \left(\frac{\varepsilon_{KN}(\gamma_c)}{\varepsilon_c} \right)^{\frac{3-p}{2}}, & \varepsilon_m^{\text{syn}} < \varepsilon_{KN}^{\text{syn}}(\gamma_c) < \varepsilon_c^{\text{syn}} \\ 1, & \varepsilon_c^{\text{syn}} < \varepsilon_{KN}^{\text{syn}}(\gamma_c), \end{cases} \quad (30)$$

with $\eta = \left(\frac{\gamma_c}{\gamma_m} \right)^{2-p}$ and $\varepsilon_{KN}^{\text{syn}}(\gamma_c) = \frac{\Gamma m_e c^2}{\gamma_c}$ (Nakar et al. 2009; Wang et al. 2010). Given the synchrotron spectral breaks $\varepsilon_m^{\text{syn}} = 2.9 \text{ eV}$, $\varepsilon_c^{\text{syn}} = 0.1 \text{ MeV}$ and $\varepsilon_{KN}^{\text{syn}}(\gamma_c) \simeq 12.8 \text{ eV}$ the Compton parameter lies in the range of $\varepsilon_m^{\text{syn}} < \varepsilon_{KN}^{\text{syn}}(\gamma_c) < \varepsilon_c^{\text{syn}}$. Solving the eq. 30, the value of $Y(\gamma_c)$ becomes ~ 0.8 .

Given the electron Lorentz factors (eq. 29) and the synchrotron spectral breaks (Sari et al. 1998), the spectral breaks and the maximum flux for SSC emission are

$$\begin{aligned} \varepsilon_m^{\text{SSC}} &\simeq 0.1 \text{ MeV} \left(\frac{1+z}{1.08} \right)^{\frac{5}{4}} \varepsilon_{e,-1.1}^4 \varepsilon_{B,-4}^{\frac{1}{2}} n^{-\frac{1}{4}} E_{51.2}^{\frac{3}{4}} t_3^{-\frac{9}{4}}, \\ \varepsilon_c^{\text{SSC}} &\simeq 6.1 \times 10^5 \text{ TeV} \left(\frac{1+z}{1.08} \right)^{-\frac{3}{4}} \left(\frac{1+Y_{\text{Th}}}{1.8} \right)^{-4} \varepsilon_{B,-4}^{-\frac{7}{2}} n^{-\frac{9}{4}} E_{51.2}^{-\frac{5}{4}} \\ &\quad \times t_3^{-\frac{1}{4}}, \\ F_{\text{max}}^{\text{SSC}} &\simeq 3.2 \times 10^{-5} \text{ mJy} \left(\frac{1+z}{1.08} \right)^{\frac{3}{4}} \varepsilon_{B,-4}^{\frac{1}{2}} n^{\frac{5}{4}} d_{z,27}^{-2} E_{51.2}^{\frac{5}{4}} t_3^{\frac{1}{4}}. \end{aligned} \quad (31)$$

The cooling spectral break is too large in comparison with the Fermi LAT energy. The SSC light curves in the fast (slow)-cooling regime are given by (Fraija et al. 2019a)

$$F_{\nu}^{\text{SSC}} \propto \begin{cases} t^{\frac{1}{8}} \varepsilon_{\gamma}^{-\frac{1}{2}} (t^{-\frac{9p-11}{8}} \varepsilon_{\gamma,11}^{-\frac{p-1}{2}}), & \varepsilon_c^{\text{SSC}}(\varepsilon_m^{\text{SSC}}) < \varepsilon_{\gamma} < \varepsilon_m^{\text{SSC}}(\varepsilon_c^{\text{SSC}}) \\ t^{-\frac{9p-10}{8}} \varepsilon_{\gamma}^{-\frac{p}{2}}, & \{\varepsilon_c^{\text{SSC}}, \varepsilon_m^{\text{SSC}}\} < \varepsilon_{\gamma}, \end{cases} \quad (32)$$

The KN suppression effect is taken into account in the SSC model because of the reduction of the emissivity in comparison with the Compton regime. The break energy in the KN regime becomes

$$\varepsilon_c^{\text{KN}} \simeq 14.3 \text{ TeV} \left(\frac{1+z}{1.08} \right)^{-\frac{3}{4}} \left(\frac{1+Y_{\text{Th}}}{1.8} \right)^{-1} \varepsilon_{B,-4}^{-1} n^{-\frac{3}{4}} E_{51.2}^{-\frac{1}{4}} \times t_3^{-\frac{1}{4}}. \quad (33)$$

5.3. H.E.S.S. detection with Fermi LAT upper limits

From the spectral breaks of synchrotron ($\varepsilon_m^{\text{syn}} \simeq 2.9 \text{ eV}$ and $\varepsilon_c^{\text{syn}} \simeq 0.1 \text{ MeV}$) and SSC ($\varepsilon_m^{\text{SSC}} \simeq 0.1 \text{ MeV}$ and $\varepsilon_c^{\text{SSC}} \simeq 6.1 \times 10^5 \text{ TeV}$) emission, one can see that at 100 MeV the synchrotron emission lies in the range $\varepsilon_m^{\text{syn}} < \varepsilon_c^{\text{syn}} < \varepsilon_{\gamma}$ and the SSC emission in the range $\varepsilon_m^{\text{SSC}} < \varepsilon_{\gamma} < \varepsilon_c^{\text{SSC}}$. It is important to consider electrons that have electron Lorentz factors γ_e^* and radiate synchrotron photons at 100 MeV. Using the electron Lorentz factor that produces synchrotron photons at the LAT regime, it is possible to obtain the critical energy $\varepsilon_{KN}^{\text{syn}}(\gamma_e^*) = \frac{\Gamma m_e c^2}{\gamma_e^*} \simeq 1.4 \text{ eV}$ (Nakar et al. 2009). In this case, the Compton parameter becomes $Y(\gamma_e^*) = Y(\gamma_c) \left(\frac{\varepsilon_{KN}^{\text{syn}}(\gamma_e^*)}{\varepsilon_{KN}^{\text{syn}}(\gamma_c)} \right)^{\frac{3-p}{2}} \simeq 0.7$ which corresponds to the range $\varepsilon_{KN}^{\text{syn}}(\gamma_e^*) < \varepsilon_m^{\text{syn}} < \varepsilon_{KN}^{\text{syn}}(\gamma_c) < \varepsilon_c^{\text{syn}}$ (Nakar et al. 2009; Wang

et al. 2010; Beniamini et al. 2015).

Therefore, the ratio of synchrotron and SSC fluxes at 100 MeV becomes

$$\frac{F_{\nu}^{\text{syn}}}{F_{\nu}^{\text{SSC}}} \sim 5.1 \left(\frac{1+z}{1.08} \right)^{-\frac{1}{4}} \left(\frac{1+Y(\gamma_e^*)}{1.7} \right)^{-1} \varepsilon_{e,-1.1}^{1-p} \varepsilon_{B,-4}^{-\frac{3}{4}} n^{-\frac{7}{6}} E_{51.2}^{-\frac{1}{12}} \Gamma_{1.5}^{\frac{5}{3}-p} t_3^{-\frac{1}{4}} \left(\frac{\varepsilon_{\gamma}}{100 \text{ MeV}} \right)^{-\frac{1}{2}}, \quad (34)$$

The ratio of the SSC to synchrotron luminosity is approximately given by $Y(\gamma_c) \equiv \frac{L_{\nu}^{\text{SSC}}}{L_{\nu}^{\text{syn}}} = \frac{U_{\text{syn}}[\varepsilon_{\gamma} < \varepsilon_{KN}^{\text{syn}}(\gamma_c)]}{U_B} \simeq 0.8$

(Wang et al. 2010). The terms U_B and $U_{\text{syn}}[\varepsilon_{\gamma} < \varepsilon_{KN}^{\text{syn}}(\gamma_c)]$ are the energy densities of the magnetic field and the synchrotron photons with energy below $\varepsilon_{KN}^{\text{syn}}(\gamma_c)$.

The right-hand panel in Figure 5 shows the SSC FS emission estimated at 100 MeV (the dashed magenta curve) and 80 GeV (the dotted-dashed green curve). The attenuation produced by the extragalactic background light (EBL) absorption is accounted for using the model presented in Franceschini and Rodighiero (2017). The intrinsic attenuation by e^{\pm} pair production is not taken into account because during the deceleration phase it is not significant. In order to verify the results of our model with the observations at high and very-high energies, the Fermi-LAT upper limits at 100 MeV and the sensitivity of H.E.S.S. at 80 GeV are shown. This panel shows that the SSC emission can reproduce the observations of H.E.S.S. and Fermi LAT (i.e., it can be detected in the H.E.S.S. observatory without being detected by the Fermi LAT instrument).

5.4. Why GRB 190829A was detectable at VHE

As follows we enumerate the reasons why this burst could have been detected.

i) *A burst located at very low redshift with intermediate luminosity.* Depending on the redshift and the photon energy, VHE flux from a generic source begins to be attenuated due to e^{\pm} pair creation with EBL photons (Gould and Schröder 1966). This attenuation can be measured through $\exp[-\tau_{\gamma\gamma}(z)]$ with $\tau_{\gamma\gamma}(z)$ the opacity. Given the distance of GRB 190829A with a low-redshift of $z \simeq 0.078$, the VHE flux at 100 GeV and 1 TeV is attenuated by a factor of 0.99 and 0.44 (Franceschini and Rodighiero 2017), respectively. On the other hand, with the best-fit parameters found after describing GRB 190829A, the SSC flux evolves in the range $\varepsilon_m^{\text{SSC}} < \varepsilon_{\gamma} < \varepsilon_c^{\text{SSC}}$ and consequently, the SSC flux varies as $\propto E^{1.1}$. Therefore, the very small attenuation factor together with an intermediate luminosity allowed that GRB 190829A could have been detected by the H.E.S.S. observatory. It is worth noting that although no imaging atmospheric Cherenkov telescope (IACT) was observing GRB 130702A, an intermediate luminosity burst with $z \lesssim 0.2$, Fermi LAT detected a GeV-photon associated with this burst (see section 5.6).

ii) *The VHE emission was released during the deceleration phase.* The high- and very-high-energy photons have been observed during the prompt and afterglow in tens of bursts (Ajello et al. 2019). Different studies of multi-wavelength observations have yielded results about the places where VHE flux is originated (e.g. internal and external shocks; Kumar and Zhang 2015). In accordance with our model and the best-fit values

found, the VHE emission reported by H.E.S.S. was created during the deceleration phase with the intrinsic attenuation due to $\gamma\gamma$ interactions much less than unity. In this case, the intrinsic attenuation did not decrease the observed SSC emission.

iii) *A favorable set of parameters.* The set of the best-fit parameters as found for GRB 190829A made more favorable its detection. For instance, with the best-fit parameters the SSC flux evolving in the second PL segment of slow-cooling regime increases as the circumburst density ($\propto n^{1.1}$) and electron equipartition parameter ($\propto \varepsilon_e^{2.3}$) increase. Higher values of these parameters make SSC emission more favorable to be detected.

iv) *The KN regime is much above hundreds of GeVs.* The electron distribution up-scatters synchrotron FS photons at the KN regime. The SSC emission evolving in the KN regime is drastically attenuated. For GRB 190829A, the SSC flux in the range of the H.E.S.S. is much below than the KN regime ($\simeq 14.3$ TeV). It allowed that the SSC flux was not attenuated and hence, was detected by the H.E.S.S. telescopes.

v) *A quick location of this burst.* To observe photons at hundreds of GeVs by IACTs has been truly a difficult challenge since these take longer in locating the burst than the duration of the main emission and the early afterglow. In spite of numerous attempts, two observations, GRB 180720B (Abdalla et al. 2019) and GRB 190114C (Acciari et al. 2019), have been possible and many upper VHE limits have been derived by these telescopes (e.g. see, Albert et al. 2007; Aleksić et al. 2014; Aharonian et al. 2009a,b; H.E.S.S. Collaboration et al. 2014; Acciari et al. 2011; Bartoli et al. 2017; Abeysekara et al. 2018). We argue that the conditions to quickly pinpoint the early afterglow of GRB 190829A by the H.E.S.S. telescope made the VHE flux detection possible.

5.5. Analysis of our SSC model for other VHE observatories

CTA Telescopes. Funk et al. (2013) and Piron (2016) presented and discussed the sensitivity to transient sources of the Cherenkov Telescope Array (CTA) telescopes for distinct energy thresholds. At 10^3 s, the CTA sensitivity for an energy threshold of 75 GeVs is $\sim 2.6 \times 10^{-10}$ mJy. In order to compare with our SSC model, the corresponding SSC flux, at $t = 10^3$ s and $\epsilon_\gamma = 75$ GeV, is $\simeq 9.0 \times 10^{-9}$ mJy. Hence, we conclude that GRB 190829A would have been detected by CTA if this would have been working. GRBs with similar characteristics of GRB 190829A are potential candidates to be detected (e.g. CTA; Funk et al. 2013).

MAGIC Telescopes. Takahashi et al. (2008) reported the MAGIC GRB sensitivity as a function of time at 100 GeV. At 10^3 s, the MAGIC sensitivity becomes $\sim 10^{-10}$ mJy. The corresponding SSC flux, at $t = 10^3$ s and $\epsilon_\gamma = 100$ GeV, would be $\simeq 7.5 \times 10^{-9}$ mJy. Therefore, we conclude that if this burst would have been early located by the MAGIC telescopes, GRB 190829A would have been detected.

HAWC Observatory. The High Altitude Water Cherenkov (HAWC) collaboration reported the GRB sensitivity as a function of time for distinct zenith angles in the energy

range of (0.1 - 1) TeV (Martinez-Castellanos 2019). Considering the zenith angle with respect of GRB 190829A ($\theta_{\text{zenith}} = 30^\circ$) at 10^3 s, the flux sensitivity is around $\simeq 10^{-8}$ erg cm $^{-2}$ s $^{-1}$. Taking into account the EBL absorption effect in the (0.1 - 1) TeV energy range, the SSC flux would be $\simeq 10^{-9}$ erg cm $^{-2}$ s $^{-1}$. We conclude that GRB 190829A could not have been detected by the HAWC gamma-ray observatory, even if this burst would have occurred during the first hours in the HAWC field of view.

5.6. Generalization to the closest ilGRBs ($z \lesssim 0.2$)

To date, there is only one confirmed ilGRB/SN detected with $z \lesssim 0.2$; GRB 130702A. GRB 130702A classified as an intermediate-luminosity burst and associated to a broad-line, type Ic supernovae SN2013dx (D’Elia et al. 2015), was detected in different wavelengths ranging from radio to high-energy gamma-rays. The Fermi GBM instrument triggered on GRB 130702A at 2013 July 02 00:05:23.079 UTC. The Fermi LAT instrument detected photons from this burst above >100 MeV within 2200 s. The duration of the main emission in the (50-300) keV energy range was $T_{90} = 59$ s and the isotropic energy reported was $6.4^{+1.3}_{-1.0} \times 10^{50}$ erg for a redshift of $z=0.145$ (Toy et al. 2016). Details of the data analysis and the afterglow observations are reported in D’Elia et al. (2015) and Toy et al. (2016).

5.6.1. Fermi-LAT analysis and synchrotron limit

The left-hand panel in Figure 6 displays the Fermi LAT energy flux (blue) and photon flux (red) light curves and upper limits obtained between 0.1 and 100 GeV. This panel shows that the flux at $\sim 10^3$ s is slightly above the upper limits at $> 10^4$ s. The right-hand panel in Figure 6 shows all the photons with energies above > 100 MeV as a function of probabilities to be associated to GRB 130702A. The data files used for this analysis are given at the data website.¹⁹ Details of the fermi tools and the procedure to analyze the Fermi LAT data are presented in Fraija et al. (2019b). Several features can be noted: i) The Fermi LAT detected three high-energy photons with probabilities $> 90\%$ of 1661, 540 and 464 MeV detected at 272, 1070 and 1818 s, respectively, after the trigger time, ii) the highest energy photon of 1661 MeV corresponded to the first photon observed at 272 s and iii) this burst displayed 5 photons above > 100 MeV with a probability less than 10% (the highest energy photon was 7 GeV).

Taking into account the value of circumburst density $n = 1$ cm $^{-3}$, the total isotropic-equivalent energy $6.4^{+1.3}_{-1.0} \times 10^{50}$ erg (D’Elia et al. 2015), the redshift of $z=0.145$ (Toy et al. 2016) and the efficiency to convert the kinetic energy into photons 0.2 (Beniamini et al. 2015), we estimate and plot the evolution of the maximum energy photon radiated by synchrotron FS model, as shown in the right-hand panel in Figure 6. It is shown that the highest energy photon detected by the Fermi LAT cannot be interpreted in the synchrotron FS scenario, an additional mechanism is required to interpret this photon. Therefore, as concluded for GRB 190829A an additional mechanism such SSC emission should be present during the FSs to explain this GeV energy photon.

¹⁹ <https://fermi.gsfc.nasa.gov/cgi-bin/ssc/LAT/LATDataQuery.cgi>

5.6.2. Parameter space so that ilGRBs can be detected by the H.E.S.S. telescopes

Using the SSC model during the FSs (eqs. 32 and 31), we compute the parameter space so that ilGRBs can be detected by the H.E.S.S. telescopes with the condition that the gamma-ray emission is below and slightly above (5 times)²⁰ the Fermi LAT sensitivity. In both cases, we consider the EBL model derived by Franceschini and Rodighiero (2017), a uniform-density medium of $n = 1 \text{ cm}^{-3}$, an electron spectral index of $p = 2.1$, a redshift of $z = 0.2$ and a deceleration time of 10^3 s .

5.6.2.1. Below the Fermi LAT sensitivity. — We plot the parameter space for which VHE gamma-ray emission can be detected in H.E.S.S. but not in the Fermi LAT. The left-hand panel in Figure 7 shows the parameter space of the microphysical parameters, isotropic-equivalent energy and the bulk Lorentz factor for which SSC flux is below the Fermi LAT sensitivity at 10 GeV and above the H.E.S.S. sensitivity at 80 GeV (Piron 2016). The upper (Γ) and the lower ($E_{\gamma, \text{iso}}$) X-axes are related through the deceleration time of 10^3 s and the density of 1 cm^{-3} . In particular, this panel shows that for $E_{\gamma, \text{iso}} \approx 10^{48} \text{ erg}$, the set of parameters that satisfy the conditions are $\epsilon_e \gtrsim 0.3$, $\epsilon_B \gtrsim 10^{-2}$, $\Gamma \sim 25$, and for $E_{\gamma, \text{iso}} \approx 10^{53} \text{ erg}$, the set of parameters become $\epsilon_e \lesssim 0.1$, $\epsilon_B \lesssim 10^{-5}$ and $\Gamma \sim 45$. It shows that VHE photons cannot be expected from ilGRBs with $\Gamma < 10$. The values of the initial Lorentz factor lies in the range of $25 \lesssim \Gamma \lesssim 45$. It is worth noting that if the deceleration time decreases about one-third of the assumed value, the initial Lorentz factor would lie in the range of $40 \lesssim \Gamma \lesssim 70$.

5.6.2.2. Slightly above the Fermi LAT sensitivity. — We plot the parameter space for which VHE gamma-ray emission can be detected in H.E.S.S. and also slightly detectable in the Fermi LAT. The right-hand panel in Figure 7 shows the parameter space of the microphysical parameters, isotropic-equivalent energy and the bulk Lorentz factor for which SSC flux is above the H.E.S.S. sensitivity at 80 GeV (Piron 2016) and slightly above the Fermi LAT sensitivity at 10 GeV. Again, the upper (Γ) and the lower ($E_{\gamma, \text{iso}}$) X-axes are related through the deceleration time of 10^3 s and the density of 1 cm^{-3} . In particular, this panel shows that for $E_{\gamma, \text{iso}} \approx 10^{48} \text{ erg}$, the set of parameters are $\epsilon_e \gtrsim 0.5$, $\epsilon_B \gtrsim 5 \times 10^{-2}$, $\Gamma \sim 28$, and for $E_{\gamma, \text{iso}} \approx 5 \times 10^{53} \text{ erg}$, the set of parameters become $\epsilon_e \lesssim 0.1$, $\epsilon_B \lesssim 10^{-5}$ and $\Gamma \sim 48$. In this case, the values of the initial Lorentz factor lies in the range of $28 \lesssim \Gamma \lesssim 48$.

6. SUMMARY

GRB 190829A, one of the closest bursts to Earth, was followed-up by a large number of satellites and observatories in several wavelengths that range from radio bands to hundreds of GeV gamma-rays. Analysis of the prompt gamma-ray emission pointed to GRB 190819A as an intermediate luminosity burst ($10^{48.5} \lesssim L_{\text{iso}} \lesssim 10^{49.5} \text{ erg}$) and modelling the X-ray and optical light curves together with its SED indicate that the outflow expands with an initial bulk Lorentz factor of $\Gamma \simeq 34$, which is high for a ilGRB (e.g.,

$\Gamma \lesssim 10$) and low for a hlGRB (e.g., $\Gamma \gtrsim 100$). Thus, GRB 190829A becomes the first intermediate-luminosity burst in being detected in the VHE gamma-ray band by an IACT, and, in turn, the first event what was not simultaneously observed by the Fermi LAT instrument. It is worth noting that the value of bulk Lorentz factor is strongly constrained by the observation of the deceleration peak and that this value is also consistent with the required range for the Lorentz factor needed to produce VHE photons via SSC without also producing an SSC signal in LAT. Our results indicate that no photons with energies above $\geq 100 \text{ MeV}$ can be associated to GRB 190829A. We found that the “plateau” phase can be interpreted as the fall-back accretion of a millisecond pulsar and the X-ray and optical observations are consistent with synchrotron forward-shock emission evolving between the characteristic and cooling spectral breaks during the early/coasting phase and late afterglow in a uniform-density medium. Using the best-fit parameters found after modelling the X-ray and optical light curves of GRB 190829A, we show that the VHE emission reported by the H.E.S.S. experiment cannot be interpreted in the synchrotron FS scenario, so that an additional mechanism should be present during the FSs to explain the multi-GeV photons. We interpret the energetic photons above the synchrotron limit in the SSC scenario during the FSs. It is worth noting that high-energy photons detected by Fermi LAT below the synchrotron limit can be explained in terms of synchrotron FS scenario. The detection of VHE emission above the synchrotron limit in GRB 190829A can be explained considering: i) the very low redshift of this burst with an intermediate luminosity, ii) their origin during the deceleration phase, iii) the favorable set of parameters, iv) the KN regime much above hundreds of GeVs and finally, v) a quick location by H.E.S.S. telescope.

To date, there is only one confirmed ilGRB/SN detected with $z \lesssim 0.2$, GRB 130702A. We have obtained the Fermi LAT light curve with its upper limits around the reported position of GRB 130702A and all photons with energies larger than $> 100 \text{ MeV}$. With a probability of $> 90\%$, three high-energy photons of 1661, 540 and 464 MeV were detected during the afterglow phase at 272, 1070 and 1818 s, respectively. It is shown that the highest energy photon cannot be interpreted in the synchrotron FS scenario, an additional mechanism is required to interpret this photon. Therefore, as concluded for GRB 190829A an additional mechanism such as SSC should be present during the FSs to explain this GeV energy photon. Considering that synchrotron FS model is not sufficient to explain the high-energy and VHE photons in the two ilGRBs, we finally compute the parameter space so that SSC flux originated in these object could be detected by the H.E.S.S. telescopes. We show that low-redshift bursts with intermediate luminosity are potential candidates to be detected in very-high energies.

NF acknowledges financial support from UNAM-DGAPA-PAPIIT through grant IA102019. RBD acknowledges support from the National Science Foundation under grant 1816694.

REFERENCES

- ²⁰ This value approximately corresponds to the difference between the upper limits derived in GRB 190829A and the observed flux in GRB 130702A.
- S. E. Woosley, *ApJ* **405**, 273 (1993).
T. J. Galama, P. M. Vreeswijk, J. van Paradijs, C. Kouveliotou, T. Augusteijn, and et al., *Nature* **395**, 670 (1998), [astro-ph/9806175](#).

- J. S. Bloom, S. R. Kulkarni, S. G. Djorgovski, A. C. Eichelberger, P. Côté, and et al., *Nature* **401**, 453 (1999), [arXiv:astro-ph/9905301 \[astro-ph\]](#).
- S. E. Woosley and J. S. Bloom, *ARA&A* **44**, 507 (2006), [astro-ph/0609142](#).
- O. Bromberg, E. Nakar, and T. Piran, *ApJ* **739**, L55 (2011), [arXiv:1107.1346 \[astro-ph.HE\]](#).
- J. Hjorth, *Philosophical Transactions of the Royal Society of London Series A* **371**, 20120275 (2013), [arXiv:1304.7736 \[astro-ph.HE\]](#).
- Z. Cano, L. Izzo, A. de Ugarte Postigo, C. C. Thöne, T. Krühler, K. E. Heintz, D. Malesani, S. Geier, C. Fuentes, T. W. Chen, S. Covino, V. D’Elia, J. P. U. Fynbo, P. Gondoni, A. Gomboc, J. Hjorth, P. Jakobsson, D. A. Kann, B. Milvang-Jensen, G. Pugliese, R. Sánchez-Ramírez, S. Schulze, J. Sollerman, N. R. Tanvir, and K. Wiersema, *A&A* **605**, A107 (2017), [arXiv:1704.05401 \[astro-ph.HE\]](#).
- S. Schulze, D. Malesani, A. Cucchiara, N. R. Tanvir, T. Krühler, A. de Ugarte Postigo, G. Leloudas, J. Lyman, D. Bersier, K. Wiersema, D. A. Perley, P. Schady, J. Gorosabel, J. P. Anderson, A. J. Castro-Tirado, S. B. Cenko, A. De Cia, L. E. Ellerbroek, J. P. U. Fynbo, J. Greiner, J. Hjorth, D. A. Kann, L. Kaper, S. Klose, A. J. Levan, S. Martín, P. T. O’Brien, K. L. Page, G. Pignata, S. Rapaport, R. Sánchez-Ramírez, J. Sollerman, I. A. Smith, M. Sparre, C. C. Thöne, D. J. Watson, D. Xu, F. E. Bauer, M. Bayliss, G. Björnsson, M. Bremer, Z. Cano, S. Covino, V. D’Elia, D. A. Frail, S. Geier, P. Gondoni, O. E. Hartoog, P. Jakobsson, H. Korhonen, K. Y. Lee, B. Milvang-Jensen, M. Nardini, A. Nicuesa Guelbenzu, M. Oguri, S. B. Pandey, G. Petitpas, A. Rossi, A. Sandberg, S. Schmidl, G. Tagliaferri, R. P. J. Tilanus, J. M. Winters, D. Wright, and E. Wuyts, *A&A* **566**, A102 (2014), [arXiv:1401.3774 \[astro-ph.HE\]](#).
- S. Campana and et al., *Nature* **442**, 1008 (2006), [astro-ph/0603279](#).
- Z. Cano, D. Bersier, C. Guidorzi, S. Kobayashi, A. J. Levan, N. R. Tanvir, K. Wiersema, P. D’Avanzo, A. S. Fruchter, P. Garnavich, A. Gomboc, J. Gorosabel, D. Kasen, D. Kopač, R. Margutti, P. A. Mazzali, A. Melandri, C. G. Mundell, P. E. Nugent, E. Pian, R. J. Smith, I. Steele, R. A. M. J. Wijers, and S. E. Woosley, *ApJ* **740**, 41 (2011), [arXiv:1104.5141 \[astro-ph.SR\]](#).
- L. Izzo, A. de Ugarte Postigo, K. Maeda, C. C. Thöne, D. A. Kann, M. Della Valle, A. Sagues Carracedo, M. J. Michałowski, P. Schady, S. Schmidl, J. Selsing, R. L. C. Starling, A. Suzuki, K. Bensc, J. Bolmer, S. Campana, Z. Cano, S. Covino, J. P. U. Fynbo, D. H. Hartmann, K. E. Heintz, J. Hjorth, J. Japelj, K. Kamiński, L. Kaper, C. Kouveliotou, M. Kruźyński, T. Kwiatkowski, G. Leloudas, A. J. Levan, D. B. Malesani, T. Michałowski, S. Piranomonte, G. Pugliese, A. Rossi, R. Sánchez-Ramírez, S. Schulze, D. Steeghs, N. R. Tanvir, K. Ulaczyk, S. D. Vergani, and K. Wiersema, *Nature* **565**, 324 (2019), [arXiv:1901.05500 \[astro-ph.HE\]](#).
- V. D’Elia, E. Pian, A. Melandri, P. D’Avanzo, M. Della Valle, P. A. Mazzali, S. Piranomonte, G. Tagliaferri, L. A. Antonelli, F. Bufano, S. Covino, D. Fugazza, D. Malesani, P. Møller, and E. Palazzi, *A&A* **577**, A116 (2015), [arXiv:1502.04883 \[astro-ph.HE\]](#).
- J. Hjorth, J. Sollerman, P. Møller, J. P. U. Fynbo, S. E. Woosley, C. Kouveliotou, N. R. Tanvir, J. Greiner, M. I. Andersen, A. J. Castro-Tirado, and et al., *Nature* **423**, 847 (2003), [astro-ph/0306347](#).
- C. Ashall, P. A. Mazzali, E. Pian, S. E. Woosley, E. Palazzi, S. J. Prentice, S. Kobayashi, S. Holmbo, A. Levan, D. Perley, M. D. Stritzinger, F. Bufano, A. V. Filippenko, A. Melandri, S. Oates, A. Rossi, J. Selsing, W. Zheng, A. J. Castro-Tirado, G. Chincarini, P. D’Avanzo, M. De Pasquale, S. Emery, A. S. Fruchter, K. Hurley, P. Møller, K. Nomoto, M. Tanaka, and A. F. Valeev, *MNRAS* **487**, 5824 (2019), [arXiv:1702.04339 \[astro-ph.HE\]](#).
- X.-Y. Wang, R.-Y. Liu, H.-M. Zhang, S.-Q. Xi, and B. Zhang, *ApJ* **884**, 117 (2019), [arXiv:1905.11312 \[astro-ph.HE\]](#).
- N. Fraija, R. Barniol Duran, S. Dichiarà, and P. Beniamini, *ApJ* **883**, 162 (2019a), [arXiv:1907.06675 \[astro-ph.HE\]](#).
- T. Piran and E. Nakar, *ApJ* **718**, L63 (2010), [arXiv:1003.5919 \[astro-ph.HE\]](#).
- A. A. Abdo, M. Ackermann, M. Ajello, K. Asano, W. B. Atwood, M. Axelsson, L. Baldini, J. Ballet, G. Barbiellini, M. G. Baring, D. Bastieri, K. Bechtol, R. Bellazzini, and et al., *ApJ* **706**, L138 (2009), [arXiv:0909.2470 \[astro-ph.HE\]](#).
- R. Barniol Duran and P. Kumar, *MNRAS* **412**, 522 (2011), [arXiv:1003.5916 \[astro-ph.HE\]](#).
- B. Zhang and P. Mészáros, *ApJ* **559**, 110 (2001), [astro-ph/0103229](#).
- N. Fraija, *ApJ* **804**, 105 (2015), [arXiv:1503.07449 \[astro-ph.HE\]](#).
- N. Fraija, W. H. Lee, M. Araya, P. Veres, R. Barniol Duran, and S. Guiriec, *ApJ* **848**, 94 (2017a), [arXiv:1709.06263 \[astro-ph.HE\]](#).
- M. Ajello, M. Arimoto, M. Axelsson, L. Baldini, G. Barbiellini, D. Bastieri, and et al., *The Astrophysical Journal* **878**, 52 (2019).
- V. A. Acciari, S. Ansoldi, L. A. Antonelli, A. A. Engels, and et al., *Nature* **575**, 459 (2019).
- H. Abdalla, R. Adam, F. Aharonian, F. Ait Benkhali, E. O. Angüner, M. Arakawa, C. Arcaro, C. Armand, H. Ashkar, M. Backes, and et al., *Nature* **575**, 464 (2019), [arXiv:1911.08961 \[astro-ph.HE\]](#).
- N. Fraija, S. Dichiarà, A. C. C. d. E. S. Pedreira, A. Galvan-Gamez, R. L. Becerra, A. Montalvo, J. Montero, B. Betancourt Kamenetskaia, and B. B. Zhang, *ApJ* **885**, 29 (2019b).
- B. Zhang, *arXiv e-prints*, [arXiv:1911.09862 \(2019\)](#), [arXiv:1911.09862 \[astro-ph.HE\]](#).
- S. Dichiarà, M. G. Bernardini, D. N. Burrows, P. D’Avanzo, C. Gronwall, J. D. Gropp, J. A. Kennea, N. J. Klingler, H. A. Krimm, N. P. M. Kuin, S. J. LaPorte, A. Melandri, K. L. Page, D. M. Palmer, M. H. Siegel, K. K. Simpson, A. Tohuvavohu, and Neil Gehrels Swift Observatory Team, *GRB Coordinates Network* **25552**, 1 (2019).
- M. de Naurois and H. E. S. S. Collaboration, *GRB Coordinates Network* **25566**, 1 (2019).
- A. de Ugarte Postigo, L. Izzo, C. C. Thöne, M. Blazek, K. Bensc, J. F. Agui, D. A. Kann, A. L. Cabrera Lavers, N. Castro-Rodriguez, and A. Tejero Caro, *GRB Coordinates Network* **25677**, 1 (2019).
- V. Chand, A. Banerjee, R. Gupta, Dimple, P. S. Pal, J. C. Joshi, B.-B. Zhang, R. Basak, P. H. T. Tam, V. Sharma, S. B. Pandey, A. Kumar, and Y.-S. Yang, *arXiv e-prints*, [arXiv:2001.00648 \(2020\)](#), [arXiv:2001.00648 \[astro-ph.HE\]](#).
- V. L. Toy, S. B. Cenko, J. M. Silverman, N. R. Butler, A. Cucchiara, A. M. Watson, D. Bersier, D. A. Perley, R. Margutti, E. Bellm, J. S. Bloom, Y. Cao, J. I. Capone, K. Clubb, A. Corsi, A. De Cia, J. A. de Diego, A. V. Filippenko, O. D. Fox, A. Gal-Yam, N. Gehrels, L. Georgiev, J. J. González, M. M. Kasliwal, P. L. Kelly, S. R. Kulkarni, A. S. Kutuyev, W. H. Lee, J. X. Prochaska, E. Ramirez-Ruiz, M. G. Richer, C. Román-Zúñiga, L. Singer, D. Stern, E. Troja, and S. Veilleux, *ApJ* **818**, 79 (2016), [arXiv:1508.00575 \[astro-ph.HE\]](#).
- D. Band, J. Matteson, L. Ford, B. Schaefter, D. Palmer, B. Teegarden, T. Cline, M. Briggs, W. Paciesas, G. Pendleton, G. Fishman, C. Kouveliotou, C. Meegan, R. Wilson, and P. LeStrade, *ApJ* **413**, 281 (1993).
- F. Piron, F. Longo, M. Axelsson, M. Arimoto, J. L. Racusin, E. Bissaldi, and Fermi-LAT Collaboration, *GRB Coordinates Network* **25574**, 1 (2019).
- S. R. Oates, S. Dichiarà, and Swift/UVOT Team, *GRB Coordinates Network* **25570**, 1 (2019).
- A. F. Valeev, A. J. Castro-Tirado, Y. D. Hu, E. Fernandez-Garcia, V. V. Sokolov, I. Carrasco, A. Castellon, D. Garcia Alvarez, M. Rivero, and et al., *GRB Coordinates Network* **25565**, 1 (2019).
- M. Fukugita, T. Ichikawa, J. E. Gunn, M. Doi, K. Shimasaku, and D. P. Schneider, *AJ* **111**, 1748 (1996).
- R. L. Becerra, A. M. Watson, N. Fraija, N. R. Butler, W. H. Lee, and et al., *ApJ* **872**, 118 (2019), [arXiv:1901.06051 \[astro-ph.HE\]](#).
- P. A. Evans, R. Willingale, J. P. Osborne, P. T. O’Brien, K. L. Page, and et al., *A&A* **519**, A102 (2010), [arXiv:1004.3208 \[astro-ph.IM\]](#).
- J. Bolmer, J. Greiner, and T. W. Chen, *GRB Coordinates Network* **25651**, 1 (2019).
- G. Terreran, W. Fong, R. Margutti, A. Miller, K. Alexander, P. Blanchard, D. Coppejans, and K. Paterson, *GRB Coordinates Network* **25664**, 1 (2019).
- J. P. Osborne, K. L. Page, M. Capalbi, M. Perri, V. D’Elia, D. N. Burrows, J. D. Gropp, A. Tohuvavohu, A. P. Beardmore, S. Dichiarà, and Swift-XRT Team, *GRB Coordinates Network* **25568**, 1 (2019).
- J. P. Norris, J. T. Bonnell, D. Kazanas, J. D. Scargle, J. Hakkila, and T. W. Giblin, *ApJ* **627**, 324 (2005), [arXiv:astro-ph/0503383 \[astro-ph\]](#).
- W. T. Vestrand, J. A. Wren, P. R. Wozniak, R. Aptekar, S. Golentskii, V. Pal’Shin, T. Sakamoto, R. R. White, S. Evans, D. Casperson, and E. Fenimore, *Nature* **442**, 172 (2006), [astro-ph/0605472](#).
- R. Brun and F. Rademakers, *Nuclear Instruments and Methods in Physics Research A* **389**, 81 (1997).
- P. N. Bhat, M. S. Briggs, V. Connaughton, C. Kouveliotou, and et al., *ApJ* **744**, 141 (2012), [arXiv:1109.4064 \[astro-ph.HE\]](#).
- R. D. Preece, M. S. Briggs, R. S. Mallozzi, G. N. Pendleton, W. S. Paciesas, and D. L. Band, *ApJ* **506**, L23 (1998), [astro-ph/9808184](#).
- B. B. Zhang, B. Zhang, A. J. Castro-Tirado, Z. G. Dai, P. H. T. Tam, and et al., *Nature Astronomy* **2**, 69 (2018), [arXiv:1612.03089 \[astro-ph.HE\]](#).
- F. Ryde, M. Axelsson, B. B. Zhang, S. McGlynn, A. Pe’er, and et al., *ApJ* **709**, L172 (2010), [arXiv:0911.2025 \[astro-ph.HE\]](#).
- P. Mészáros and M. J. Rees, *ApJ* **530**, 292 (2000), [arXiv:astro-ph/9908126 \[astro-ph\]](#).
- P. Beniamini and T. Piran, *MNRAS* **445**, 3892 (2014), [arXiv:1402.4113 \[astro-ph.HE\]](#).
- P. Beniamini, D. Giannios, and B. D. Metzger, *MNRAS* **472**, 3058 (2017), [arXiv:1706.05014 \[astro-ph.HE\]](#).

- P. Beniamini, R. Barniol Duran, and D. Giannios, *MNRAS* **476**, 1785 (2018), [arXiv:1801.04944 \[astro-ph.HE\]](#).
- M. V. Medvedev, *ApJ* **540**, 704 (2000), [arXiv:astro-ph/0001314 \[astro-ph\]](#).
- A. Spitkovsky, *ApJ* **682**, L5 (2008a), [arXiv:0802.3216](#).
- A. Spitkovsky, *ApJ* **673**, L39 (2008b), [arXiv:0706.3126 \[astro-ph\]](#).
- F. Ryde and A. Pe'er, *ApJ* **702**, 1211 (2009), [arXiv:0811.4135 \[astro-ph\]](#).
- Z. L. Uhm and B. Zhang, *Nature Physics* **10**, 351 (2014), [arXiv:1303.2704 \[astro-ph.HE\]](#).
- A. Lazarian, B. Zhang, and S. Xu, *ApJ* **882**, 184 (2019), [arXiv:1801.04061 \[astro-ph.HE\]](#).
- A. Pe'er, P. Mészáros, and M. J. Rees, *ApJ* **652**, 482 (2006), [astro-ph/0603343](#).
- D. Lazzati and M. C. Begelman, *ApJ* **725**, 1137 (2010), [arXiv:1005.4704 \[astro-ph.HE\]](#).
- I. Vurm and A. M. Beloborodov, *ApJ* **831**, 175 (2016), [arXiv:1506.01107 \[astro-ph.HE\]](#).
- B. Ahlgren, J. Larsson, T. Nymark, F. Ryde, and A. Pe'er, *MNRAS* **454**, L31 (2015), [arXiv:1506.02926 \[astro-ph.HE\]](#).
- P. Beniamini and D. Giannios, *MNRAS* **468**, 3202 (2017), [arXiv:1703.07380 \[astro-ph.HE\]](#).
- G. Chincarini, A. Moretti, P. Romano, A. D. Falcone, D. Morris, and et al., *ApJ* **671**, 1903 (2007), [arXiv:astro-ph/0702371 \[astro-ph\]](#).
- K. A. Arnaud, in *Astronomical Data Analysis Software and Systems V*, Astronomical Society of the Pacific Conference Series, Vol. 101, edited by G. H. Jacoby and J. Barnes (1996) p. 17.
- J. M. Lattimer and B. F. Schutz, *ApJ* **629**, 979 (2005), [arXiv:astro-ph/0411470 \[astro-ph\]](#).
- R. A. Chevalier, *ApJ* **346**, 847 (1989).
- S. E. Woosley and A. Heger, *ApJ* **752**, 32 (2012), [arXiv:1110.3842 \[astro-ph.HE\]](#).
- E. Quataert and D. Kasen, *MNRAS* **419**, L1 (2012), [arXiv:1105.3209 \[astro-ph.HE\]](#).
- B. D. Metzger, P. Beniamini, and D. Giannios, *ApJ* **857**, 95 (2018), [arXiv:1802.07750 \[astro-ph.HE\]](#).
- A. L. Piro and C. D. Ott, *ApJ* **736**, 108 (2011), [arXiv:1104.0252 \[astro-ph.HE\]](#).
- K. Parfrey, A. Spitkovsky, and A. M. Beloborodov, *ApJ* **822**, 33 (2016), [arXiv:1507.08627 \[astro-ph.HE\]](#).
- S. Campana, M. Colpi, S. Mereghetti, L. Stella, and M. Tavani, *A&A Rev.* **8**, 279 (1998), [arXiv:astro-ph/9805079 \[astro-ph\]](#).
- E.-W. Liang, S.-X. Yi, J. Zhang, H.-J. Lü, B.-B. Zhang, and B. Zhang, *ApJ* **725**, 2209 (2010), [arXiv:0912.4800 \[astro-ph.HE\]](#).
- G. Ghirlanda, L. Nava, G. Ghisellini, A. Celotti, D. Burlon, S. Covino, and A. Melandri, *MNRAS* **420**, 483 (2012), [arXiv:1107.4096 \[astro-ph.HE\]](#).
- N. Bucciantini, E. Quataert, B. D. Metzger, T. A. Thompson, J. Arons, and L. Del Zanna, *MNRAS* **396**, 2038 (2009), [arXiv:0901.3801 \[astro-ph.HE\]](#).
- B. D. Metzger, D. Giannios, T. A. Thompson, N. Bucciantini, and E. Quataert, *MNRAS* **413**, 2031 (2011), [arXiv:1012.0001 \[astro-ph.HE\]](#).
- R. Sari, T. Piran, and R. Narayan, *ApJ* **497**, L17 (1998), [arXiv:astro-ph/97112005](#).
- R. Sari and T. Piran, *A&AS* **138**, 537 (1999a), [astro-ph/9901105](#).
- R. Sari and T. Piran, *ApJ* **520**, 641 (1999b), [astro-ph/9901338](#).
- H. Gao, W.-H. Lei, Y.-C. Zou, X.-F. Wu, and B. Zhang, *New Astronomy Reviews* **57**, 141 (2013), [arXiv:1310.2181 \[astro-ph.HE\]](#).
- S.-X. Yi, X.-F. Wu, and Z.-G. Dai, *ApJ* **776**, 120 (2013), [arXiv:1308.6095 \[astro-ph.HE\]](#).
- S. Kobayashi, *ApJ* **545**, 807 (2000), [astro-ph/0009319](#).
- R. A. Chevalier and Z.-Y. Li, *ApJ* **536**, 195 (2000), [arXiv:astro-ph/9908272](#).
- A. Panaitescu and P. Kumar, *ApJ* **543**, 66 (2000), [astro-ph/0003246](#).
- N. Fraija, F. De Colle, P. Veres, S. Dichiara, R. Barniol Duran, A. Galvan-Gamez, and A. C. d. E. S. Pedreira, *ApJ* **871**, 123 (2019c).
- N. Fraija, W. H. Lee, P. Veres, and R. Barniol Duran, *ApJ* **831**, 22 (2016a).
- P. T. O'Brien, R. Willingale, J. Osborne, M. R. Goad, K. L. Page, and et al., *ApJ* **647**, 1213 (2006), [astro-ph/0601125](#).
- L.-Y. Huang, X.-G. Wang, W. Zheng, E.-W. Liang, D.-b. Lin, and et al., *ApJ* **859**, 163 (2018), [arXiv:1804.02104 \[astro-ph.HE\]](#).
- E. McMahon, P. Kumar, and A. Panaitescu, *MNRAS* **354**, 915 (2004), [arXiv:astro-ph/0404588 \[astro-ph\]](#).
- C. D. Dermer and K. E. Mitman, "External Shock Model for the Prompt Phase of Gamma Ray Bursts: Implications for GRB Source Models," in *Third Rome Workshop on Gamma-Ray Bursts in the Afterglow Era ASP*, Astronomical Society of the Pacific Conference Series, Vol. 312, edited by M. Feroci, F. Frontera, N. Masetti, and L. Piro (2004) p. 301.
- J. M. Burgess, D. Bégué, F. Ryde, N. Omodei, A. Pe'er, J. L. Racusin, and A. Cucchiara, *ApJ* **822**, 63 (2016), [arXiv:1506.05131 \[astro-ph.HE\]](#).
- V. Z. Golkhou and N. R. Butler, *ApJ* **787**, 90 (2014), [arXiv:1403.4254 \[astro-ph.HE\]](#).
- E. Nakar and R. Sari, *ApJ* **747**, 88 (2012), [arXiv:1106.2556 \[astro-ph.HE\]](#).
- J. C. Tan, C. D. Matzner, and C. F. McKee, *ApJ* **551**, 946 (2001), [astro-ph/0012003](#).
- R. Sari and P. Mészáros, *ApJ* **535**, L33 (2000), [arXiv:astro-ph/0003406 \[astro-ph\]](#).
- B. Zhang, Y. Z. Fan, J. Dyks, S. Kobayashi, P. Mészáros, D. N. Burrows, J. A. Nousek, and N. Gehrels, *ApJ* **642**, 354 (2006), [astro-ph/0508321](#).
- R. Barniol Duran, E. Nakar, T. Piran, and R. Sari, *MNRAS* **448**, 417 (2015), [arXiv:1407.4475 \[astro-ph.HE\]](#).
- N. Fraija, A. C. d. E. S. Pedreira, and P. Veres, *ApJ* **871**, 200 (2019d).
- P. Beniamini and R. Mochkovitch, *A&A* **605**, A60 (2017), [arXiv:1705.03900 \[astro-ph.HE\]](#).
- P. Beniamini, R. Duque, F. Daigne, and R. Mochkovitch, *MNRAS* **492**, 2847 (2020), [arXiv:1907.05899 \[astro-ph.HE\]](#).
- P. Kumar and B. Zhang, *Phys. Rep.* **561**, 1 (2015), [arXiv:1410.0679 \[astro-ph.HE\]](#).
- E. V. Derishev, V. V. Kocharovsky, and V. V. Kocharovsky, *ApJ* **521**, 640 (1999).
- N. Fraija, *ApJ* **787**, 140 (2014), [arXiv:1401.1581 \[astro-ph.HE\]](#).
- A. M. Beloborodov, *ApJ* **585**, L19 (2003), [arXiv:astro-ph/0209228 \[astro-ph\]](#).
- Y. Z. Fan and D. M. Wei, *MNRAS* **364**, L42 (2005), [astro-ph/0506155](#).
- N. Fraija, W. Lee, and P. Veres, *ApJ* **818**, 190 (2016b), [arXiv:1601.01264 \[astro-ph.HE\]](#).
- N. Fraija, P. Veres, B. B. Zhang, R. Barniol Duran, R. L. Becerra, B. Zhang, W. H. Lee, A. M. Watson, C. Ordaz-Salazar, and A. Galvan-Gamez, *ApJ* **848**, 15 (2017b), [arXiv:1705.09311 \[astro-ph.HE\]](#).
- N. Fraija and P. Veres, *ApJ* **859**, 70 (2018), [arXiv:1804.02449 \[astro-ph.HE\]](#).
- P. Beniamini and P. Kumar, *MNRAS* **457**, L108 (2016), [arXiv:1510.03873 \[astro-ph.HE\]](#).
- Planck Collaboration, N. Aghanim, Y. Akrami, M. Ashdown, J. Aumont, C. Baccigalupi, M. Ballardini, and A. J. e. a. Bandy, *arXiv e-prints*, [arXiv:1807.06209 \(2018\)](#), [arXiv:1807.06209 \[astro-ph.CO\]](#).
- F. James and M. Roos, *Comput. Phys. Commun.* **10**, 343 (1975).
- M. G. Bernardini, S. Campana, G. Ghisellini, P. D'Avanzo, D. Burlon, S. Covino, G. Ghirlanda, A. Melandri, R. Salvaterra, S. D. Vergani, V. D'Elia, D. Fugazza, B. Sbarufatti, and G. Tagliaferri, *ApJ* **775**, 67 (2013), [arXiv:1306.0013 \[astro-ph.HE\]](#).
- P. Beniamini, L. Nava, R. B. Duran, and T. Piran, *MNRAS* **454**, 1073 (2015), [arXiv:1504.04833 \[astro-ph.HE\]](#).
- B. Zhang and A. Pe'er, *ApJ* **700**, L65 (2009), [arXiv:0904.2943 \[astro-ph.HE\]](#).
- H. Gao and B. Zhang, *ApJ* **801**, 103 (2015), [arXiv:1409.3584 \[astro-ph.HE\]](#).
- C. Lundman, A. Pe'er, and F. Ryde, *MNRAS* **428**, 2430 (2013), [arXiv:1208.2965 \[astro-ph.HE\]](#).
- I. Vurm, A. M. Beloborodov, and J. Poutanen, *ApJ* **738**, 77 (2011), [arXiv:1104.0394 \[astro-ph.HE\]](#).
- P. Veres, B.-B. Zhang, and P. Mészáros, *ApJ* **761**, L18 (2012), [arXiv:1208.1790 \[astro-ph.HE\]](#).
- S. Guiricé, R. Mochkovitch, T. Piran, F. Daigne, C. Kouveliotou, J. Racusin, N. Gehrels, and J. McEnery, *ApJ* **814**, 10 (2015), [arXiv:1507.06976 \[astro-ph.HE\]](#).
- P. Beniamini and J. Granot, *MNRAS* **459**, 3635 (2016), [arXiv:1509.02192 \[astro-ph.HE\]](#).
- P. Kumar and A. Panaitescu, *ApJ* **541**, L51 (2000), [astro-ph/0006317](#).
- B.-B. Zhang, B. Zhang, E.-W. Liang, and X.-Y. Wang, *ApJ* **690**, L10 (2009), [arXiv:0808.3793 \[astro-ph\]](#).
- A. M. Beloborodov, F. Daigne, R. Mochkovitch, and Z. L. Uhm, *MNRAS* **410**, 2422 (2011), [arXiv:1003.1265 \[astro-ph.HE\]](#).
- R. Barniol Duran, M. Leng, and D. Giannios, *MNRAS* **455**, L6 (2016), [arXiv:1509.02521 \[astro-ph.HE\]](#).
- R. Barniol Duran and P. Kumar, *MNRAS* **395**, 955 (2009), [arXiv:0806.1226 \[astro-ph\]](#).
- M. R. Goad, K. L. Page, O. Godet, A. Beardmore, J. P. Osborne, and et al., *A&A* **468**, 103 (2007), [arXiv:astro-ph/0612661 \[astro-ph\]](#).
- S. D. Barthelmy, J. K. Cannizzo, N. Gehrels, G. Cusumano, V. Mangano, and et al., *ApJ* **635**, L133 (2005), [arXiv:astro-ph/0511576 \[astro-ph\]](#).
- G. Tagliaferri, M. Goad, G. Chincarini, A. Moretti, S. Campana, and et al., *Nature* **436**, 985 (2005), [arXiv:astro-ph/0506355 \[astro-ph\]](#).
- L. Amati, F. Frontera, M. Tavani, and et al., *A&A* **390**, 81 (2002), [arXiv:astro-ph/0205230 \[astro-ph\]](#).
- L. Amati, *MNRAS* **372**, 233 (2006), [arXiv:astro-ph/0601553 \[astro-ph\]](#).
- Z. Cano, A. de Ugarte Postigo, A. Pozanenko, N. Butler, C. C. Thöne, and et al., *A&A* **568**, A19 (2014), [arXiv:1405.3114 \[astro-ph.HE\]](#).

- V. D’Elia, S. Campana, A. D’Ài, M. De Pasquale, S. W. K. Emery, and et al., *A&A* **619**, A66 (2018), [arXiv:1810.03339 \[astro-ph.HE\]](#).
- P. Kumar and R. Barniol Duran, *MNRAS* **400**, L75 (2009), [arXiv:0905.2417 \[astro-ph.HE\]](#).
- G. Vedrenne and J.-L. Atteia, *Gamma-Ray Bursts: The Brightest Explosions in the Universe*, 2009 (2009).
- X.-Y. Wang, H.-N. He, Z. Li, X.-F. Wu, and Z.-G. Dai, *ApJ* **712**, 1232 (2010), [arXiv:0911.4189 \[astro-ph.HE\]](#).
- E. Nakar, S. Ando, and R. Sari, *ApJ* **703**, 675 (2009), [arXiv:0903.2557 \[astro-ph.HE\]](#).
- A. Franceschini and G. Rodighiero, *A&A* **603**, A34 (2017), [arXiv:1705.10256 \[astro-ph.HE\]](#).
- R. J. Gould and G. Schröder, *Phys. Rev. Lett.* **16**, 252 (1966).
- M. Ajello, M. Arimoto, M. Axelsson, L. Baldini, G. Barbiellini, and et al., *ApJ* **878**, 52 (2019), [arXiv:1906.11403 \[astro-ph.HE\]](#).
- J. Albert, E. Aliu, H. Anderhub, P. Antoranz, A. Armada, C. Baixeras, and et al., *ApJ* **667**, 358 (2007), [astro-ph/0612548](#).
- J. Aleksić, S. Ansoldi, L. A. Antonelli, P. Antoranz, A. Babic, U. Barres de Almeida, and et al., *MNRAS* **437**, 3103 (2014), [arXiv:1311.3637 \[astro-ph.HE\]](#).
- F. Aharonian, A. G. Akhperjanian, U. Barres de Almeida, A. R. Bazer-Bachi, B. Behera, W. Benbow, and et al., *A&A* **495**, 505 (2009a), [arXiv:0901.2187 \[astro-ph.HE\]](#).
- F. Aharonian, A. G. Akhperjanian, U. Barres DeAlmeida, A. R. Bazer-Bachi, B. Behera, M. Beilicke, and et al., *ApJ* **690**, 1068 (2009b), [arXiv:0809.2334](#).
- H.E.S.S. Collaboration, A. Abramowski, F. Aharonian, F. Ait Benkhali, A. G. Akhperjanian, E. Angüner, G. Anton, S. Balenderan, A. Balzer, A. Barnacka, and et al., *A&A* **565**, A16 (2014), [arXiv:1405.0488 \[astro-ph.HE\]](#).
- V. A. Acciari, E. Aliu, T. Arlen, T. Aune, M. Beilicke, W. Benbow, and et al., *ApJ* **743**, 62 (2011), [arXiv:1109.0050 \[astro-ph.HE\]](#).
- B. Bartoli, P. Bernardini, X. J. Bi, Z. Cao, S. Catalanotti, S. Z. Chen, and et al., *ApJ* **842**, 31 (2017), [arXiv:1703.09284 \[astro-ph.HE\]](#).
- A. U. Abeysekara, A. Archer, W. Benbow, R. Bird, R. Brose, M. Buchovecky, and et al., *ArXiv e-prints* (2018), [arXiv:1803.01266 \[astro-ph.HE\]](#).
- S. Funk, J. A. Hinton, and CTA Consortium, *Astroparticle Physics* **43**, 348 (2013), [arXiv:1205.0832 \[astro-ph.HE\]](#).
- F. Piron, *Comptes Rendus Physique* **17**, 617 (2016), [arXiv:1512.04241 \[astro-ph.HE\]](#).
- K. Takahashi, K. Murase, K. Ichiki, S. Inoue, and S. Nagataki, *ApJ* **687**, L5 (2008), [arXiv:0806.2825](#).
- I. Martinez-Castellanos, *ArXiv e-prints*, [arXiv:1908.06122](#) (2019), [arXiv:1908.06122 \[astro-ph.HE\]](#).
- H. A. Krimm, K. Yamaoka, S. Sugita, M. Ohno, T. Sakamoto, and et al., *ApJ* **704**, 1405 (2009), [arXiv:0908.1335 \[astro-ph.HE\]](#).

TABLE 1
SPECTRAL ANALYSIS USING THE GBM DATA

Time Interval (s)	α_{Band}	β_{Band}	E_{peak} (keV)	E_{iso} (erg)	F (erg cm $^{-2}$ s $^{-1}$)
Initial pulse^a					
[-2.0 ; 0.0]	-0.10 ± 0.02	-1.32 ± 0.10	11.4 ± 1.7	$(3.0 \pm 0.2) \times 10^{49}$	$(2.22 \pm 0.31) \times 10^{-7}$
[0.0 ; 2.0]	-0.72 ± 0.45	-1.80 ± 0.08	62.3 ± 25.1	$(3.7 \pm 0.2) \times 10^{49}$	$(6.41 \pm 0.39) \times 10^{-7}$
[2.0 ; 4.0]	-1.15 ± 0.25	-2.53 ± 0.41	59.0 ± 12.4	$(1.1 \pm 0.1) \times 10^{49}$	$(3.05 \pm 0.34) \times 10^{-7}$
[4.0 ; 6.0]	-0.10 ± 0.02	-2.15 ± 0.13	20.5 ± 4.3	$(7.3 \pm 0.4) \times 10^{48}$	$(1.79 \pm 0.24) \times 10^{-7}$
[6.0 ; 8.0]	-0.10 ± 0.02	-2.50 ± 0.38	15.1 ± 3.9	$(2.9 \pm 0.2) \times 10^{48}$	$(7.30 \pm 0.81) \times 10^{-8}$
[8.0 ; 10.0]	-0.10 ± 0.02	-2.38 ± 0.32	11.4 ± 1.7	$(2.0 \pm 0.1) \times 10^{48}$	$(4.69 \pm 0.16) \times 10^{-8}$
[10.0 ; 12.0]	-0.10 ± 0.02	-2.50 ± 0.38	15.2 ± 10.4	$(1.0 \pm 0.1) \times 10^{48}$	$(2.61 \pm 0.77) \times 10^{-8}$
Brighter peak^b					
[46.0 ; 48.0]	-1.11 ± 0.17	-2.20 ± 0.18	14.0 ± 9.9	$(5.1 \pm 0.1) \times 10^{48}$	$(1.09 \pm 0.21) \times 10^{-7}$
[48.0 ; 50.0]	-1.18 ± 0.93	-2.46 ± 0.03	12.0 ± 2.3	$(4.7 \pm 0.1) \times 10^{49}$	$(9.47 \pm 0.03) \times 10^{-7}$
[50.0 ; 52.0]	-1.11 ± 1.12	-2.48 ± 0.02	10.8 ± 2.6	$(7.4 \pm 0.1) \times 10^{49}$	$(1.47 \pm 0.03) \times 10^{-6}$
[52.0 ; 54.0]	-0.82 ± 1.46	-2.50 ± 0.02	11.1 ± 2.0	$(6.5 \pm 0.1) \times 10^{49}$	$(1.34 \pm 0.02) \times 10^{-6}$
[54.0 ; 56.0]	-1.19 ± 1.22	-2.58 ± 0.04	10.0 ± 3.9	$(4.6 \pm 0.1) \times 10^{49}$	$(8.44 \pm 0.21) \times 10^{-7}$
[56.0 ; 58.0]	-1.11 ± 0.17	-2.58 ± 0.05	8.9 ± 1.3	$(2.82 \pm 0.03) \times 10^{49}$	$(4.92 \pm 0.17) \times 10^{-7}$
[58.0 ; 60.0]	-1.11 ± 0.17	-2.64 ± 0.09	9.7 ± 1.6	$(1.43 \pm 0.02) \times 10^{49}$	$(2.54 \pm 0.15) \times 10^{-7}$
[60.0 ; 62.0]	-1.11 ± 0.17	-2.66 ± 0.13	7.1 ± 4.2	$(8.4 \pm 0.1) \times 10^{48}$	$(1.27 \pm 0.13) \times 10^{-7}$
[62.0 ; 64.0]	-1.11 ± 0.17	-2.50 ± 0.17	11.5 ± 1.7	$(5.2 \pm 0.1) \times 10^{48}$	$(1.05 \pm 0.16) \times 10^{-7}$
[64.0 ; 66.0]	-1.11 ± 0.17	-2.29 ± 0.29	11.5 ± 1.7	$(2.52 \pm 0.03) \times 10^{48}$	$(5.20 \pm 1.78) \times 10^{-8}$
[66.0 ; 68.0]	-1.11 ± 0.17	-2.55 ± 0.38	20.6 ± 10.8	$(1.81 \pm 0.02) \times 10^{48}$	$(4.33 \pm 0.94) \times 10^{-8}$

^a The total isotropic-equivalent energy and the peak energy correspond to $(9.151 \pm 0.504) \times 10^{49}$ erg and 67.88 \pm 23.34 keV, respectively.

^b The total isotropic-equivalent energy and the peak energy correspond to $(2.967 \pm 0.032) \times 10^{50}$ erg and 11.47 \pm 0.36 keV, respectively.

TABLE 2
THE BEST-FIT PARAMETERS FROM THE INITIAL PULSE AND THE BRIGHTER PEAK DISPLAYED IN THE GBM LIGHT CURVE

Event	Period	τ_1	τ_2	α_γ	t_0	χ^2/ndf
	(s)	(s)	(s)		(s)	
Initial pulse	[-2.0 ; 10]	2.31 ± 0.06	0.39 ± 0.10	—	0.11 ± 0.06	0.81
Brighter peak	[46 ; 68]	32.2 ± 7.2	—	6.59 ± 1.65	43.6 ± 9.1	0.84

TABLE 3
THE BEST-FIT PARAMETERS OBTAINED FROM THE UVOT LIGHT CURVES. THE THEORETICAL VALUES ARE ESTIMATED FOR $p = 2.15 \pm 0.17$.

Band	Rise index/Theory	Peak time	Decay index/Theory	$\Delta t/t$	F_{cont}	χ^2/ndf
	$-(\alpha_{\text{O},r})$	$t_{\text{br}} (\times 10^3 \text{ s})$	$(\alpha_{\text{O},d})$		$(\times 10^{-2} \text{ mJy})$	
V	$3.28 \pm 0.43 / 3.0$	1.39 ± 0.30	$1.19 \pm 0.30 / 0.86 \pm 0.13$	1.01 ± 0.22	5.58 ± 0.45	0.87
B	$2.87 \pm 0.41 / 3.0$	1.41 ± 0.32	$1.13 \pm 0.38 / 0.86 \pm 0.13$	0.68 ± 0.21	2.56 ± 0.34	1.25
White	$3.08 \pm 0.31 / 3.0$	1.38 ± 0.29	$1.03 \pm 0.25 / 0.86 \pm 0.13$	0.71 ± 0.23	1.31 ± 0.25	1.71
U	$2.80 \pm 0.32 / 3.0$	1.25 ± 0.39	$0.76 \pm 0.22 / 0.86 \pm 0.13$	0.73 ± 0.23	0.93 ± 0.09	0.81

TABLE 4
THE BEST-FIT PARAMETER OBTAINED FROM DIFFERENT EPOCHS IDENTIFIED IN THE SWIFT (BAT + XRT) LIGHT CURVE. THE THEORETICAL VALUES ARE ESTIMATED FOR $p = 2.15 \pm 0.17$.

Epochs	Period	Index/Theory	Peak time (s)	$\Delta t/t$	χ^2/ndf
0	52 – 62 s	$2.72 \pm 0.28/3.1 \pm 0.15$	–	–	0.75
I	82 – 215 s	$3.53 \pm 0.70 / 3.1 \pm 0.15$	–	–	0.81
II	215 – 700 s	$0.06 \pm 0.01 / 0$	–	–	0.84
III	$700 - 1.4^{+0.17}_{-0.15} \times 10^5$ s	$-(3.12 \pm 0.94) / -3.0$ $1.03 \pm 0.12 / 0.86 \pm 0.13$	1.4×10^3	0.75 ± 0.24	0.83
IV ^a	$\geq 1.4^{+0.17}_{-0.15} \times 10^5$ s	$1.23 \pm 0.04 / 1.11 \pm 0.13$	–	–	0.91

^a These values are taken from the Swift analysis.

TABLE 5
THE BEST-FIT PARAMETERS OF THE MULTI-PEAKS OBTAINED FROM THE XRT LIGHT CURVE AT 10 keV.

Peaks	Index (α_X)	Peak time (s)	$\Delta t/t$	χ^2/ndf
a	$-(22.9 \pm 6.2)$ 3.5 ± 1.3	97.5	0.15	1.7
b	$-(11.0 \pm 0.9)$ 13.05 ± 1.5	133.0	0.14	1.1
c	$-(25.6 \pm 3.5)$ 6.8 ± 1.6	172.0	0.12	1.4
d	$-(16.3 \pm 3.4)$ 16.4 ± 5.9	208.0	0.14	0.1
e	$-(19.7 \pm 3.2)$ 9.1 ± 7.1	253.0	0.17	0.1
f	$-(11.7 \pm 9.1)$ 3.3 ± 2.1	364.0	0.12	0.2
g	$-(8.9 \pm 5.2)$ 5.3 ± 2.4	401.0	0.16	0.2
h	$-(7.9 \pm 6.5)$ 5.8 ± 2.7	508.0	0.22	0.6
i	$-(19.9 \pm 3.8)$ 10.2 ± 2.5	840.0	0.11	0.5

TABLE 6
THE BEST-FIT PARAMETERS OF THE XRT SPECTRUM USING A PL AND A PL PLUS A BB MODEL. THE FIRST LINE IN EACH TIME WINDOW CORRESPONDS TO THE BEST-FIT PARAMETERS WITH THE PL AND THE SECOND ONE WITH THE PL PLUS THE BB MODEL.

Time Window	$n_H \times 10^{22}$	Spectral Index	KT	Reduced	f_{BB}/f_{BL}
(s)	(cm^{-2})	β	(keV)	χ^2	
100 - 150	$0.37^{+0.12}_{-0.10}$	$2.19^{+0.12}_{-0.10}$	-	1.19	-
	$0.17^{+0.29}_{-0.17}$	$2.10^{+1.80}_{-1.19}$	$0.65^{+0.16}_{-0.11}$	1.16	0.8621
150 - 200	$0.66^{+0.26}_{-0.20}$	$2.29^{+0.35}_{-0.32}$	-	1.24	-
	$0.08^{+0.08}_{-0.08}$	-3.00^{+err}_{-err}	$0.67^{+0.07}_{-0.04}$	1.20	2.52
200 - 230	$1.26^{+0.67}_{-0.49}$	$2.46^{+0.60}_{-0.53}$	-	0.76	-
	$3.32^{+2.2}_{-1.5}$	$-3.39^{+1.06}_{-0.46}$	$0.07^{+0.01}_{-0.02}$	0.75	389.27
250 - 299	$1.97^{+1.21}_{-0.92}$	$3.02^{+1.13}_{-0.97}$	-	0.95	-
	$3.49^{+3.05}_{-2.55}$	5.61^{+err}_{-err}	$1.76^{+1.24}_{-0.95}$	0.96	0.001
300 - 499	$1.25^{+0.38}_{-0.32}$	$2.64^{+0.44}_{-0.41}$	-	1.13	-
	$1.40^{+1.32}_{-0.92}$	$3.63^{+3.03}_{-3.38}$	$0.86^{+95.5}_{-0.64}$	1.16	0.07
500 - 700	$1.00^{+0.35}_{-0.29}$	$2.58^{+0.47}_{-0.44}$	-	0.80	-
	$1.52^{+0.97}_{-0.92}$	$4.69^{+1.95}_{-2.57}$	$0.92^{+0.81}_{-0.34}$	0.76	0.02
700 - 900	$1.37^{+0.43}_{-0.36}$	$2.55^{+0.42}_{-0.39}$	-	1.36	-
	$1.07^{+1.07}_{-0.77}$	$2.32^{+2.83}_{-2.72}$	$0.63^{+0.26}_{-0.19}$	1.34	0.18
1000 - 1200	$0.91^{+0.14}_{-0.13}$	$2.05^{+0.16}_{-0.15}$	-	1.15	-
	$0.91^{+0.31}_{-0.30}$	$2.17^{+0.64}_{-1.03}$	$1.16^{+0.91}_{-0.24}$	1.15	0.01
1200 - 1299	$0.79^{+0.12}_{-0.12}$	$1.87^{+0.14}_{-0.13}$	-	1.16	-
	$0.94^{+0.18}_{-0.16}$	$1.98^{+0.16}_{-0.15}$	$0.05^{+0.01}_{-0.01}$	1.14	14.76
1300 - 1399	$0.98^{+0.13}_{-0.12}$	$2.08^{+0.14}_{-0.13}$	-	1.19	-
	$0.49^{+0.33}_{-0.24}$	$1.29^{+0.66}_{-1.31}$	$0.63^{+0.11}_{-0.08}$	1.19	0.53
1400 - 1500	$1.09^{+0.15}_{-0.14}$	$2.21^{+0.15}_{-0.14}$	-	1.24	-
	$0.43^{+0.32}_{-0.18}$	$1.05^{+0.79}_{-1.59}$	$0.64^{+0.07}_{-0.07}$	1.19	0.91
1500 - 1599	$0.93^{+0.13}_{-0.11}$	$2.05^{+0.13}_{-0.13}$	-	1.44	-
	$0.73^{+0.26}_{-0.25}$	$1.71^{+0.56}_{-0.60}$	$0.51^{+0.28}_{-0.24}$	1.44	0.16
1600 - 1700	$1.20^{+0.15}_{-0.14}$	$2.20^{+0.14}_{-0.14}$	-	1.26	-
	$0.88^{+0.33}_{-0.34}$	$1.79^{+0.48}_{-0.87}$	$0.59^{+0.37}_{-0.11}$	1.30	0.23

TABLE 7
THE BEST-FIT PARAMETERS FOUND FROM THE MULTI-WAVELENGTH OBSERVATIONS.

Parameter	Values
Spin-down Magnetar	
$B (\times 10^{16} \text{ G})$	3.0 ± 0.3
$P (10^{-3} \text{ s})$	1.2 ± 0.1
$t_{\text{fb}} (\text{s})$	$(1.5 \pm 0.2) \times 10^4$
Synchrotron FS model	
$\varepsilon_B (10^{-4})$	1.1 ± 0.1
$\varepsilon_e (10^{-1})$	0.8 ± 0.1
p	2.3 ± 0.2
$n (10^{-1} \text{ cm}^{-3})$	1.0 ± 0.1
$E (10^{51} \text{ erg})$	2.4 ± 0.2

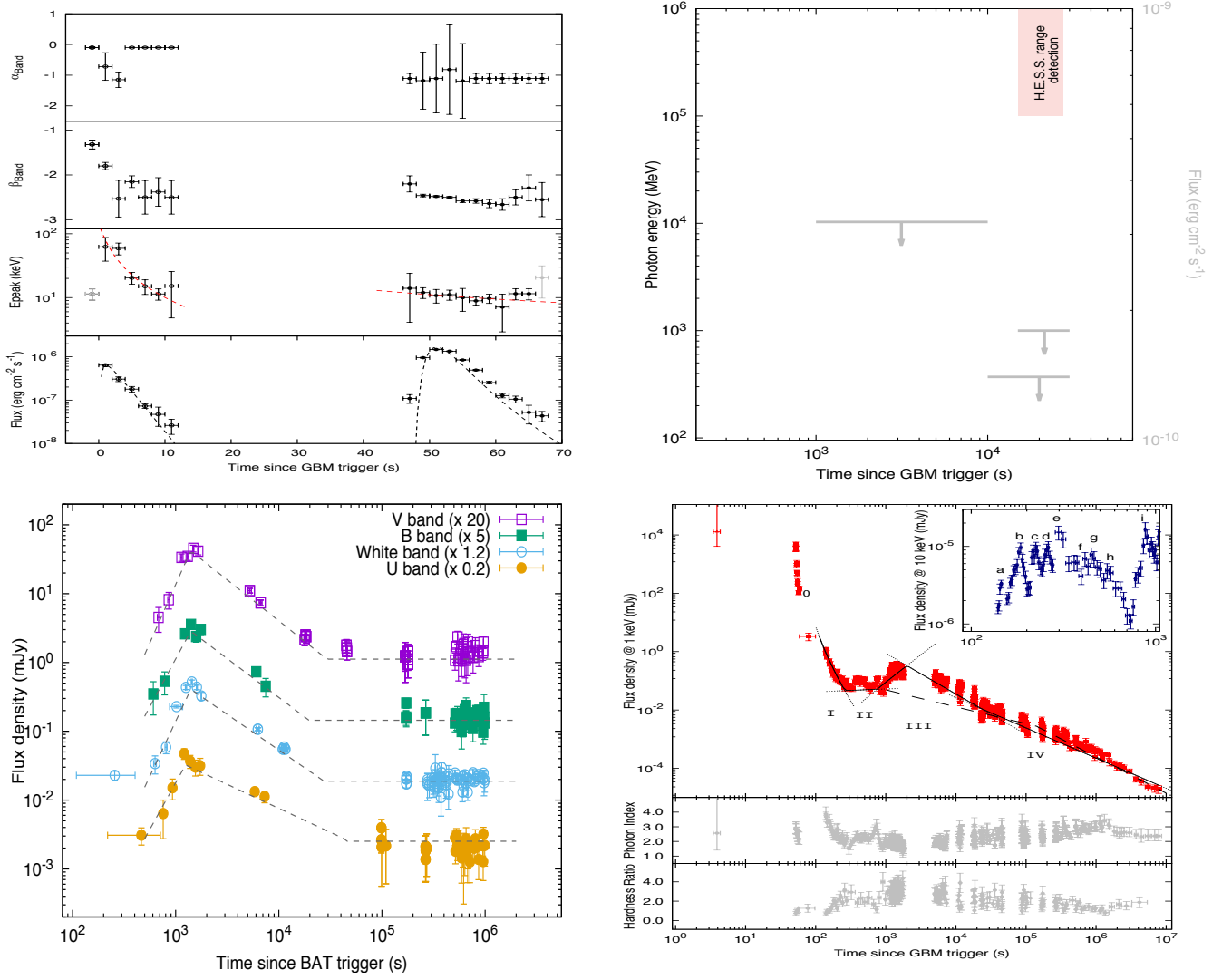


FIG. 1.— The upper left-hand panel shows the gamma-ray light curve and the evolution of the peak energy, the low-energy and high-energy spectral indexes of GRB 190829A. From top to bottom: the low-energy spectral index, the high-energy spectral index, the energy peak and the gamma-ray light curve obtained in the 10 - 1000 keV energy range. The initial gamma-ray pulse is shown in open circles and the brighter peak in filled circles. Lines in all panels correspond to the best-fit functions. Fermi GBM data are reduced using the public database at their respective websites. The upper right-hand panel shows Fermi LAT upper limits and all the photons with energies above 100 MeV with different probabilities of being associated to GRB 190829A. The lower left-hand panel shows the Swift UVOT light curve in the V, B, White and U bands. The dashed grey curves in all color filters correspond to the best-fit BPL functions. Swift UVOT data are reduced using the public database at the official Swift web site. The lower right-hand panel shows the X-ray light curve at 1 keV and the small box at 10 keV. At 1 keV five phases are labeled: “0” the initial PL segment, “I” the steep decay, “II” the plateau phase, “III” X-ray flare and “IV” the canonical normal decay and at 10 keV nine small peaks are labeled: “a”, “b”, “c”, “d”, “e”, “f”, “g”, “h” and “i”. The best-fit curves are drawn in each phase. The middle sub-panel corresponds to the photon index light curves and the bottom sub-panel the hardness ratio light curve. The solid lines in black corresponds to the best-fit curves found in this work and the dashed lines in gray represent the best-fit curves reported by Swift team.

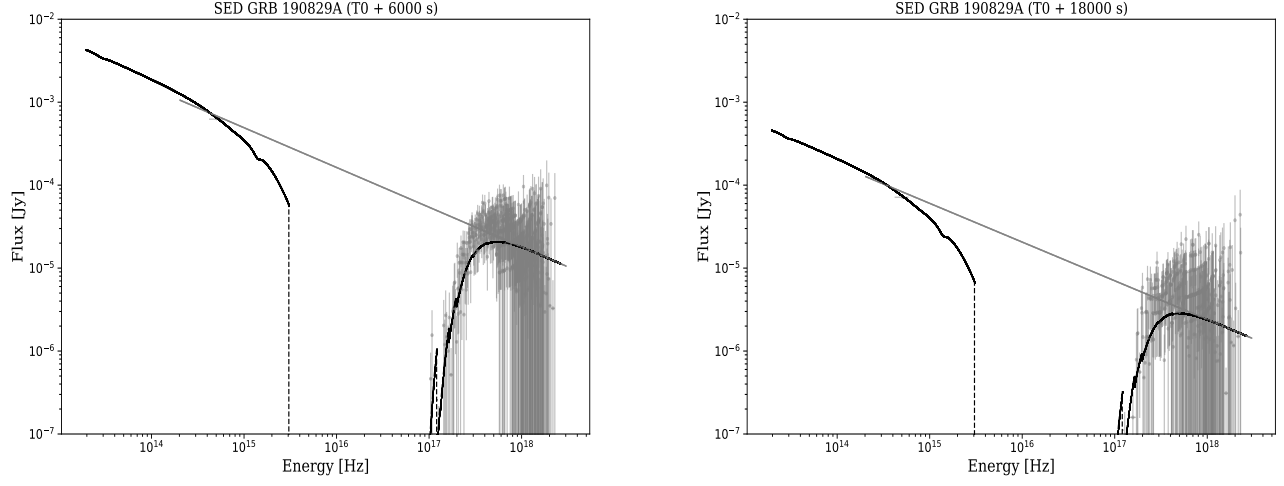


FIG. 2.— The broadband SEDs of the X-ray and optical observations at 6000 s (left) and 18000 s (right) are shown (epoch “III”). The dashed gray lines in each panel correspond to the best-fit curve from XSPEC.

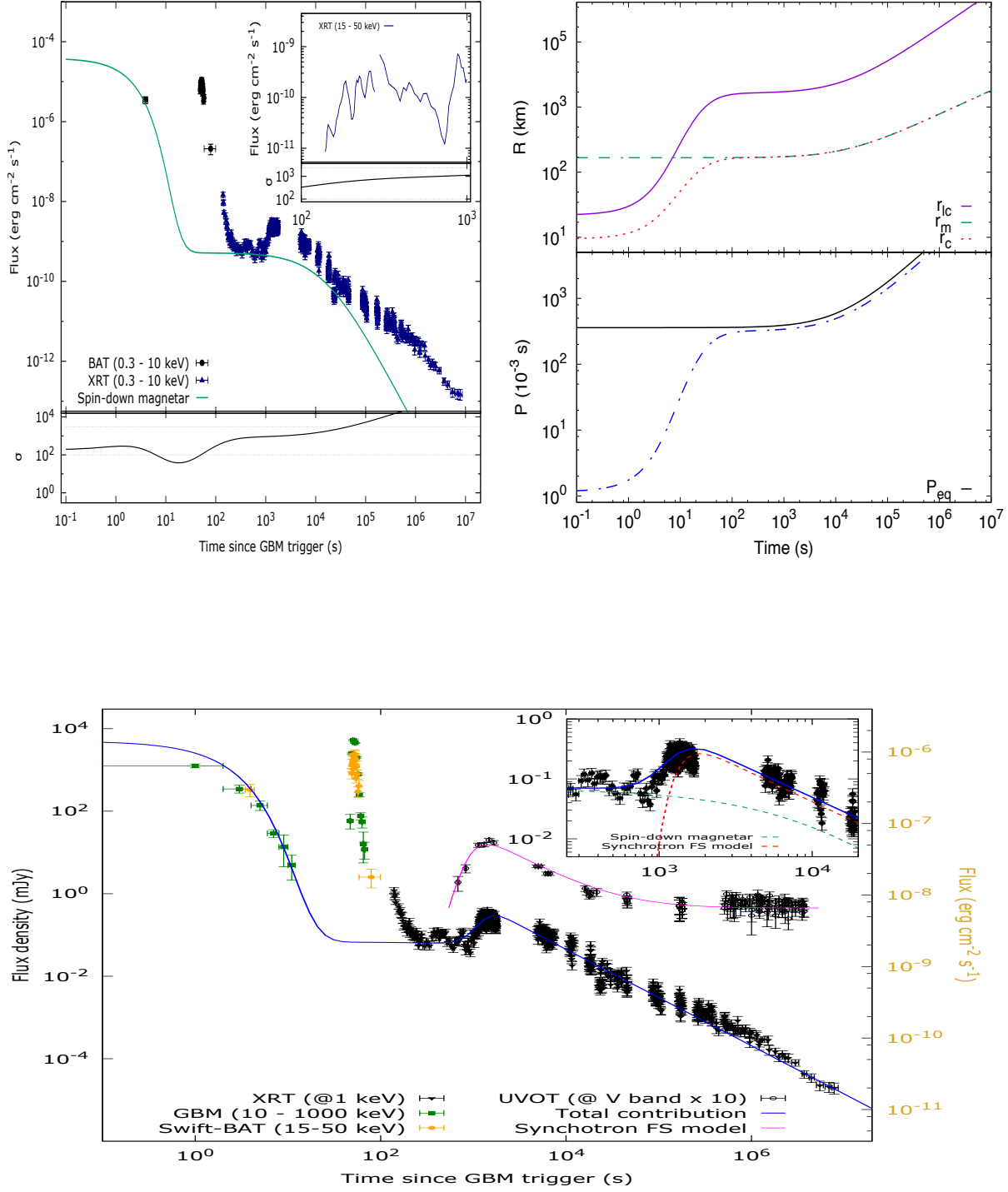


FIG. 3.— Upper left-hand panel shows the X-ray light curve with the best-fit curve given by the spin-down magnetar (above) and the evolution of the magnetization parameter (above). The small box shows the lightcurve at 10 keV. The upper right-hand panel shows the evolution of the Alfvén (r_m), co-rotation (r_c) and the light cylinder (r_{lc}) radii (above) and the evolution of the spin period (below). The lower panel shows the multi-wavelength light curves of GRB 190829A with the best-fit curves given by the spin-down magnetar and the synchrotron FS model.

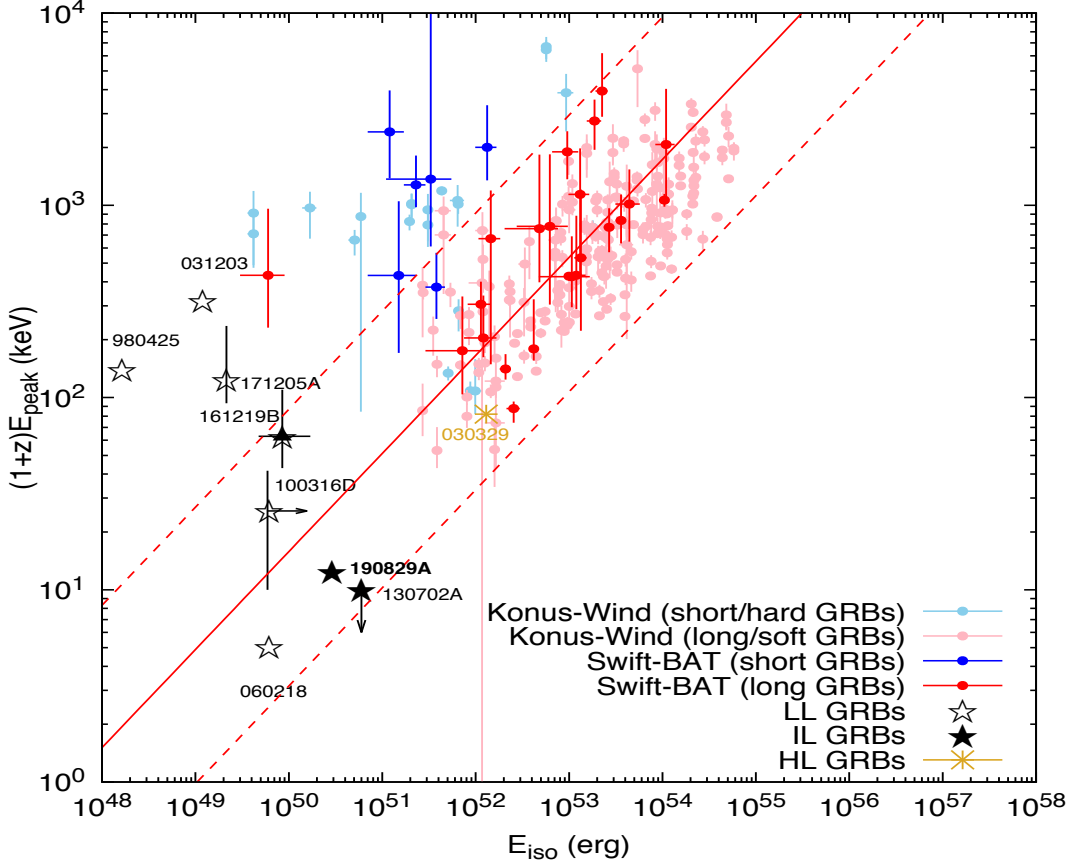


FIG. 4.— The E_{peak} and E_{iso} relation for GRB detected by Konus-Wind, Swift BAT and low-luminosity GRB samples. This figure is adapted from [D'Elia et al. \(2018\)](#). The black filled star in bold face shows GRB 190829A. The solid and dashed red lines correspond to the best fit and vertical logarithmic deviations (2.5σ), respectively, reported in ([Krimm et al. 2009](#)). The E_{peak} and E_{iso} of LL, IL and HLGRBs are obtained from GRB 980425/ SN 1998bw ([Galama et al. 1998](#)), GRB 060218/ SN 2006aj ([Campana and et al. 2006](#)), GRB 100316D/ SN 2010bh ([Cano et al. 2011](#)), GRB 161219B/ SN 2016jca ([Cano et al. 2017](#); [Ashall et al. 2019](#)), GRB 171205A/ SN 2017iuk ([Izzo et al. 2019](#)), GRB 130702A/ SN 2013dx ([D'Elia et al. 2015](#)) and GRB 030329/ SN 2003dh ([Hjorth et al. 2003](#)).

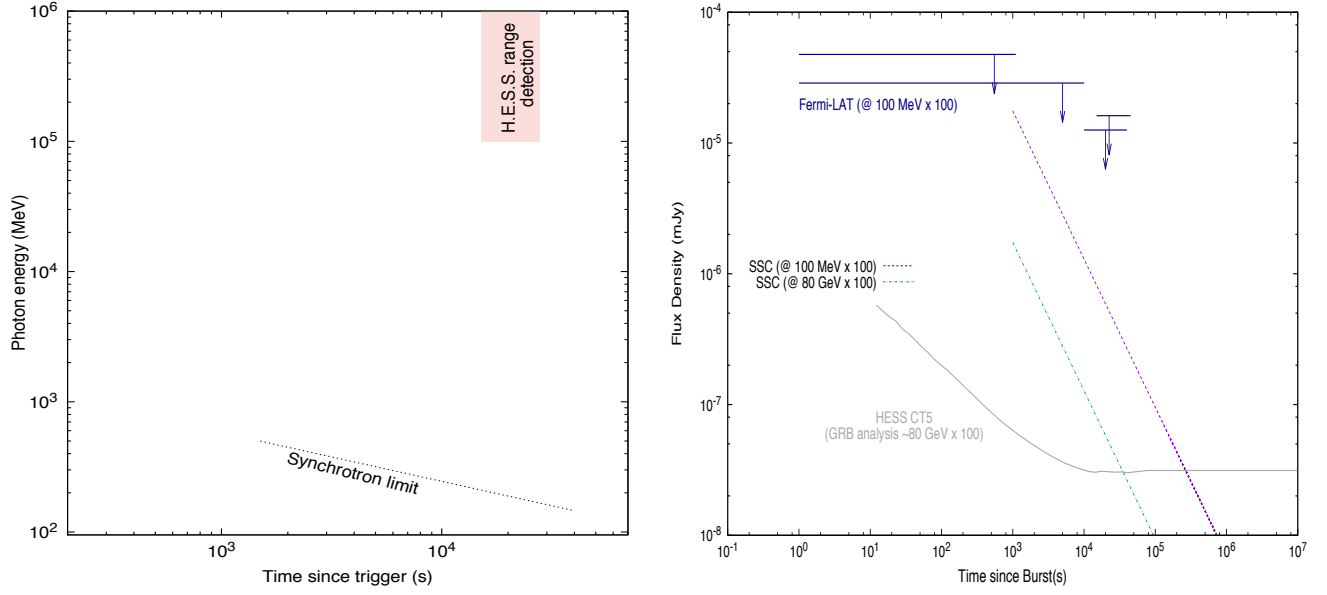


FIG. 5.— The left-hand panel shows the interval and the energy range of VHE photons reported by the H.E.S.S. Collaboration (the pink region) and the synchrotron limit (the dashed line). The right-hand panel shows the SSC emission estimated at 100 MeV and 80 GeV from the forward- and reverse-shock model computed from the deceleration of the wide jet in a circumburst medium with uniform density. In order to verify our model with the observations at high and very-high energies, the Fermi-LAT upper limits at 100 MeV and the sensitivity of H.E.S.S. at 80 GeV. (Piron 2016).

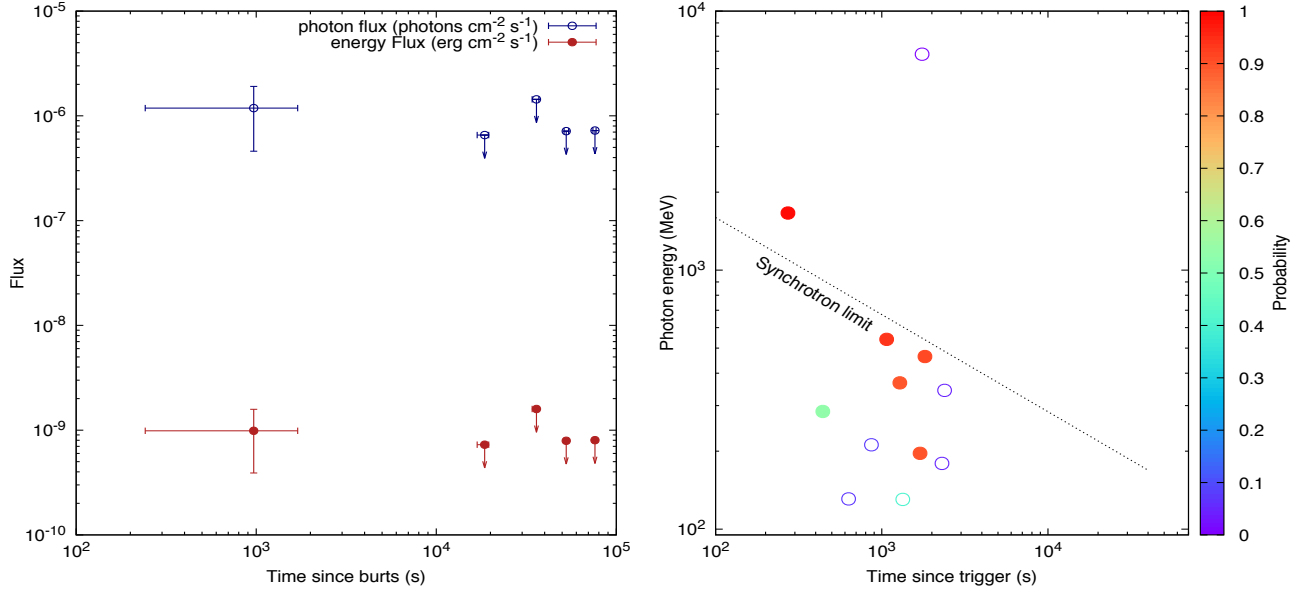


FIG. 6.— The left-hand panel shows the Fermi-LAT energy flux (blue) and photon flux (red) light curves obtained between 0.1 and 100 GeV. The right-hand panel shows all the photons with energies > 100 MeV and their respective probabilities to be associated to GRB 130702A. The dotted line corresponds to the synchrotron limit.

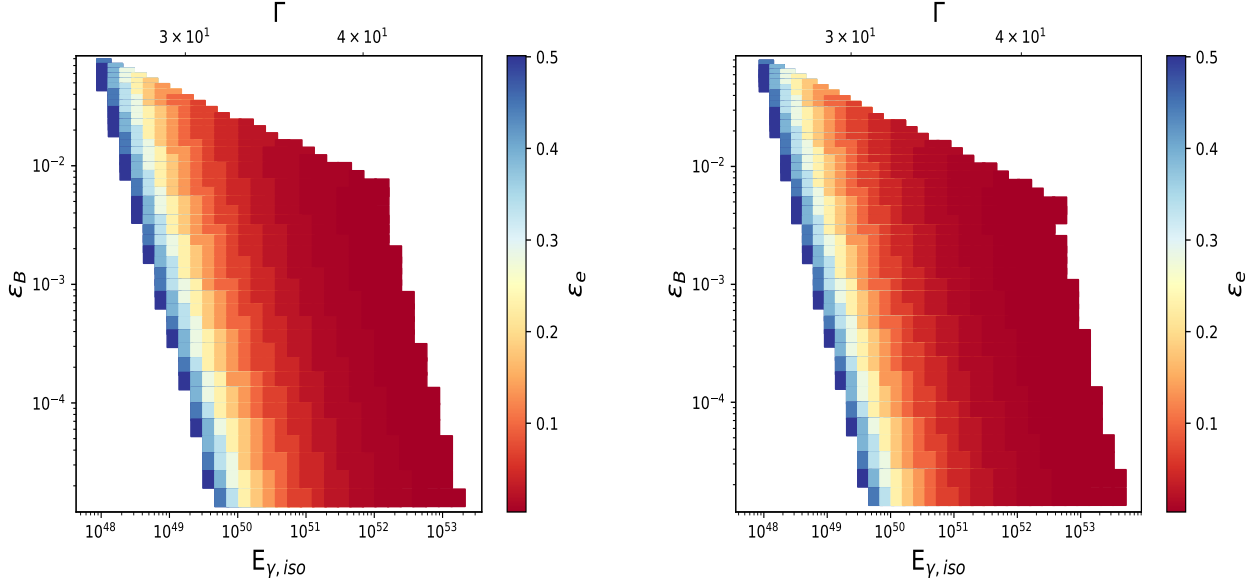


FIG. 7.— The left-hand panel shows the 4D parameter space of the microphysical parameters, isotropic energy and bulk Lorentz factor for which SSC flux from FS is below (left) and above 5 times (right) the LAT sensitivity at 10 GeV and above the H.E.S.S. sensitivity at 80 GeV (Piron 2016). The upper (Γ) and the lower ($E_{\gamma, iso}$) X-axes are related through the deceleration time of 10^3 s and the density of 1 cm^{-3} .